Chapter 35 – FINAL RESULTS OF THE INTERNATIONAL VORTEX FLOW EXPERIMENT – RESUMÉ AND OUTLOOK

by

Dietrich Hummel *(Retired)*

35.1 SUMMARY

At the end of the RTO-phase of the Second International Vortex Flow Experiment (VFE-2) the up to now achieved experimental and numerical results on the vortical flow about a delta wing with sharp and blunt leading edges are summarized, and special attention is called to the present status of knowledge. Some problems, which could not be solved within VFE-2, are also mentioned and the needs for further investigations are stressed in an outlook.

35.2 INTRODUCTION

The Second International Vortex Flow Experiment (VFE-2) has been carried out on a flat plate delta wing according to Figure 35-1 with interchangeable leading edges, one sharp and three blunt ones [35-1], [35-2]. The experimental and numerical investigations were mainly concentrated on the medium radius blunt leading edge (MRLE) configuration and on the sharp leading edge (SLE) case for comparison [35-3], see Chapter 17.

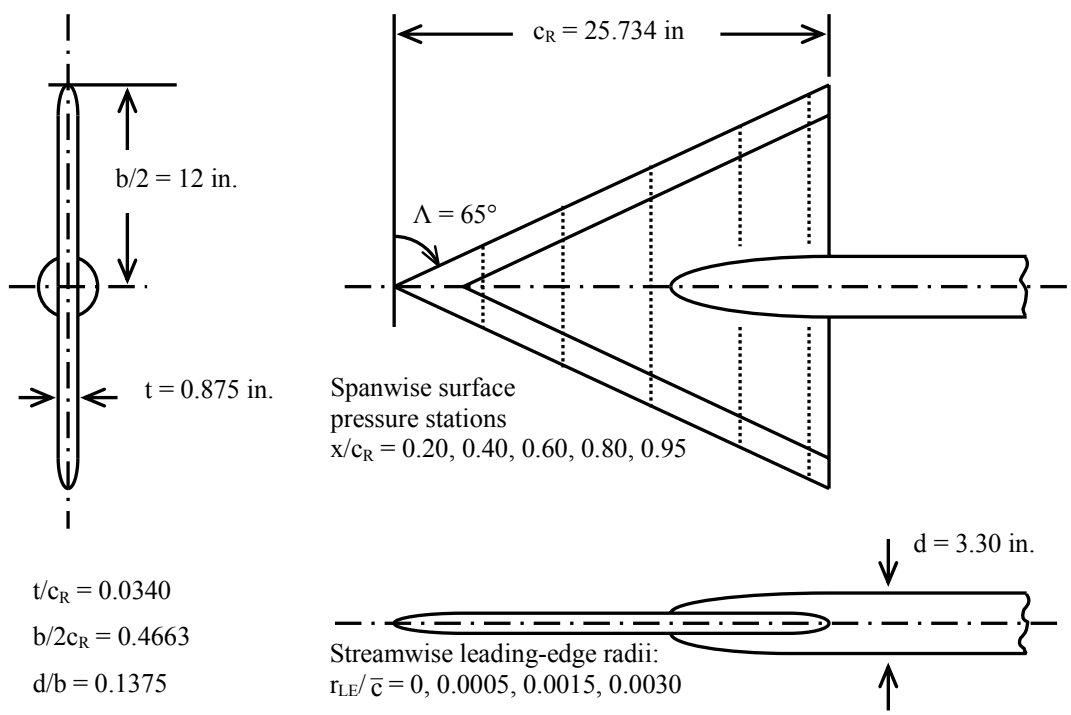

Figure 35-1: VFE-2 Configuration: NASA Delta Wing Λ = 65° According to [35-1].

The geometry of the VFE-2 configuration looks very simple, but the details of the shape indicate some geometric properties, which have to be noticed:

i) In the apex region the ratio of local thickness to half-span d/b_{loc} reaches considerable values and this means that a thickness distribution is present there, which may cause local flow separations. This applies for sharp and for blunt leading edges.

ii) For blunt leading edges the curvature radius r_{LE} is constant along the leading edge. Therefore the ratio r_{LE}/b_{loc} reduces along the leading edge from the apex of the wing towards the trailing edge. This means that the leading edge becomes sharper downstream, and this again favours flow separations.

In the subsequent discussion of the results of the VFE-2 these geometric peculiarities have to be born in mind. A special configuration has been investigated both experimentally and numerically. From the results many conclusions about the aerodynamic behaviour of slender bodies with rounded leading edges may be drawn, but not all aerodynamic problems related to blunt bodies with low aspect ratio are covered properly by the VFE-2 data sets.

35.3 FULLY SEPARATED FLOW WITHOUT VORTEX BREAKDOWN

In this section the results for the VFE-2 configuration at *angle of attack* $\alpha = 18°$ are discussed. For sharp and medium radius rounded leading edge the flow is fully separated along the whole leading edge. This is the standard case of a vortical flow around this configuration.

35.3.1 Overall Forces and Moments

The experiments at NASA [35-4], ONERA and TUBITAK-SAGE [35-6], see Chapters 18, 20, 23 and 24, have shown, that there exist only minor differences between the SLE and the MRLE configuration concerning the normal force coefficient as indicated in Figure 35-2. However, the centre of pressure of the blunt-edged wing is located slightly more forward compared to the sharp-edged wing [35-9] and in addition the blunt-edged wing produces a larger forward facing axial force than the sharp-edged wing due to the suction area in the leading edge region, see Figure 35-2.

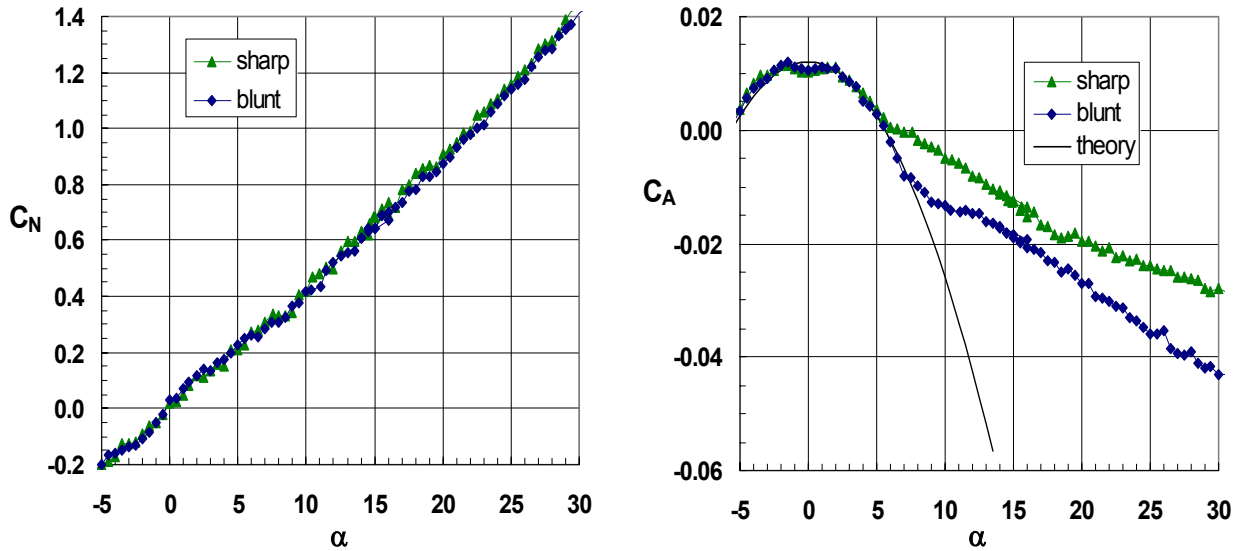

Figure 35-2: Effect of Bluntness on Experimental Normal and Axial Force Coefficients for the VFE-2 Configuration with Sharp (SLE) and Medium Radius Rounded Leading Edge (MRLE) at M = 0.1, R_{mac} = 1 x 10^6. Results from ONERA L1 [[35-6] and Chapter 20].

35.3.2 Pressure Distributions

All CFD codes available within VFE-2 have been applied to the most simple case of fully developed vortical flow at α = 18°. Some results for SLE [35-11], [35-15], see Chapter 25, 30 and 34, are shown in Figure 35-3 and Figure 35-4. In general the experimental data are covered properly by the numerical solutions, but in the region of maximum suction and in the secondary vortex area some deviations are visible, which might be due to different turbulence models used.

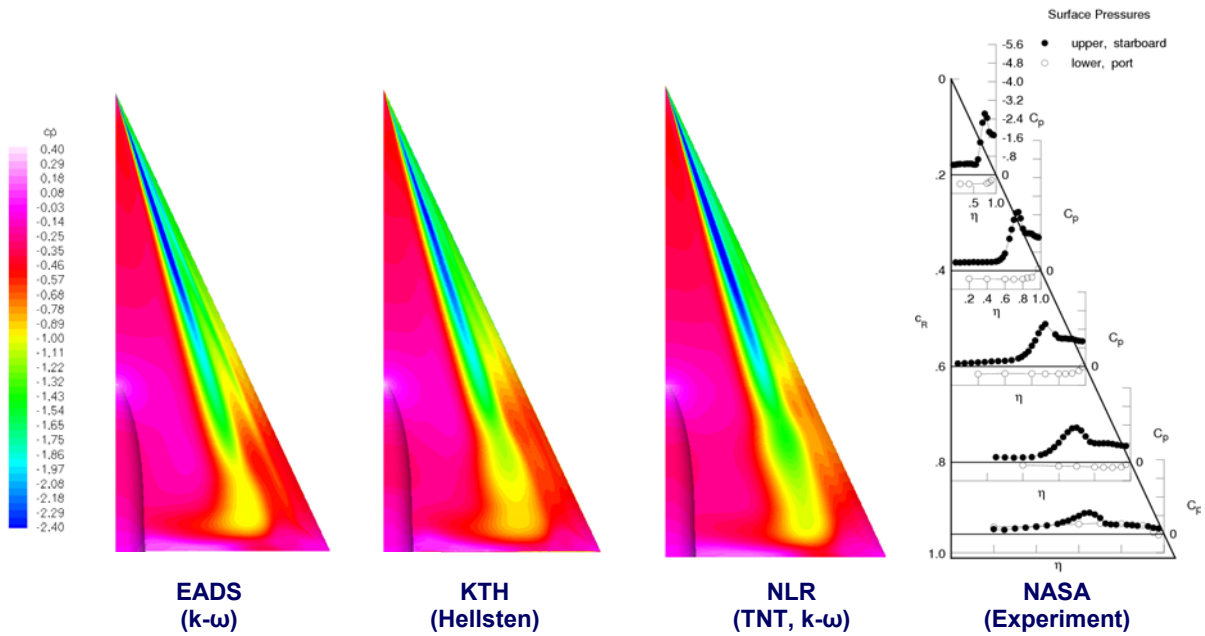

Figure 35-3: Surface Pressure Distribution on the VFE-2 Configuration with Sharp Leading Edges (SLE) at M = 0.40, α = 18°, Re = 6 x 10^6 [[35-17] and Chapter 34].

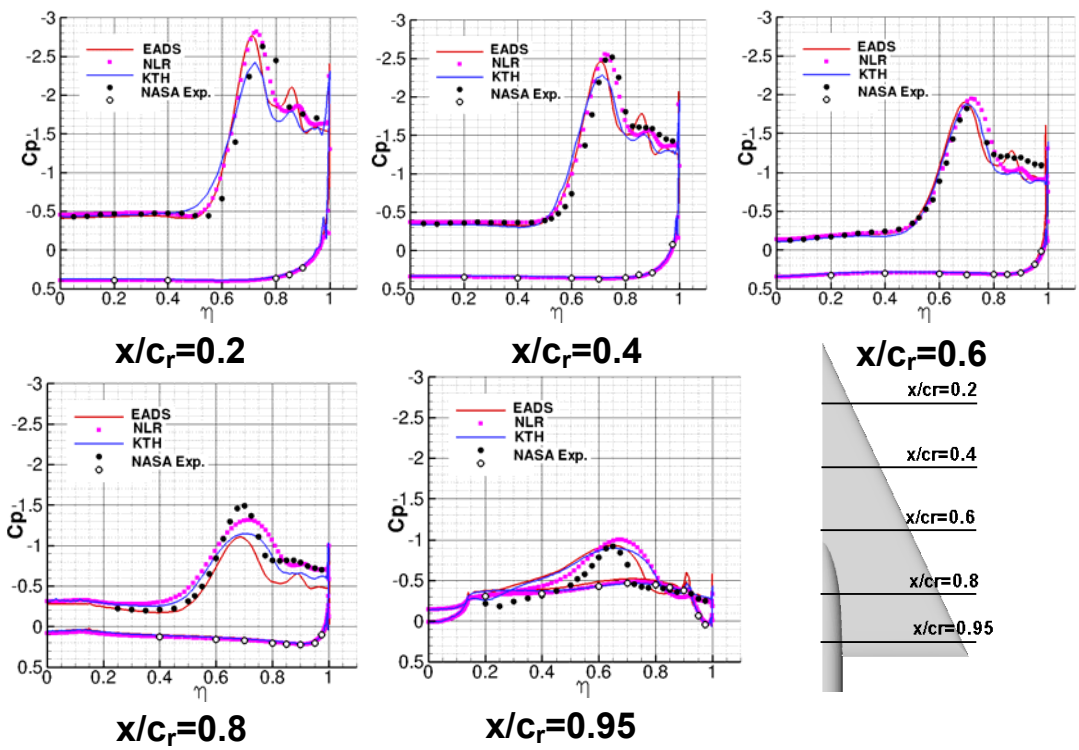

Figure 35-4: Comparison of Calculated Surface Pressures with Experimental Data for the VFE-2 Configuration with Sharp Leading Edges (SLE) at M = 0.40, α = 18°, Re = 6 x 10^6 [[35-17] and Chapter 34].

Corresponding results for the medium radius rounded leading edge (MRLE) configuration [35-11], [35-12], [35-14], [35-15], [35-16], see Chapters 25, 28, 30, 31 and 32, are presented in Figure 35-5 and Figure 35-6. Also for this configuration reasonable agreement between the experiments and the various numerical results turned out, but again the question of correct turbulence modeling remains.

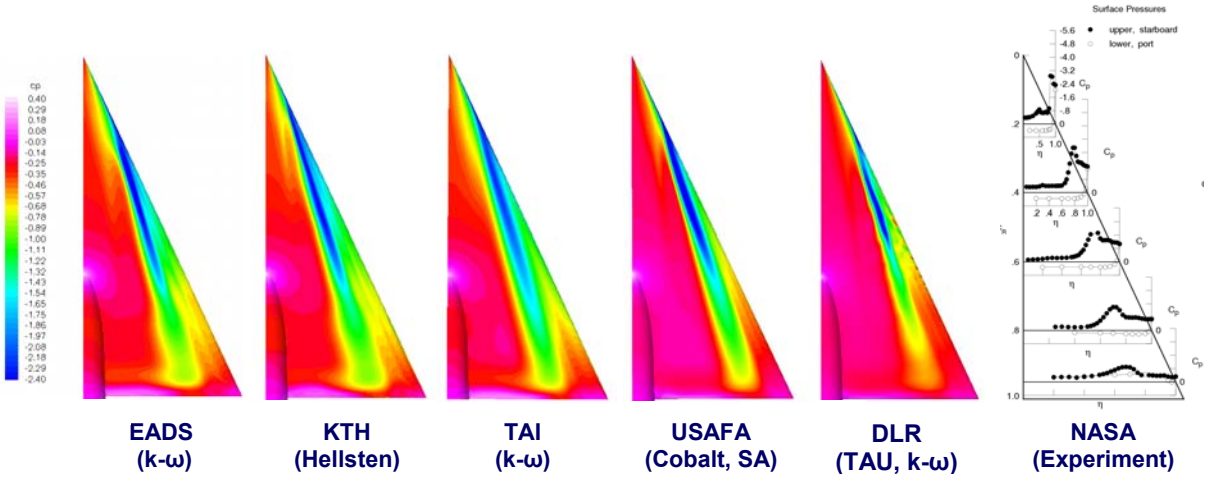

Figure 35-5: Surface Pressure Distribution on the VFE-2 Configuration with Medium Radius Rounded Leading Edges (MRLE) at M = 0.40, α = 18°, Re = 6 x 10^6 [[35-17] and Chapter 34].

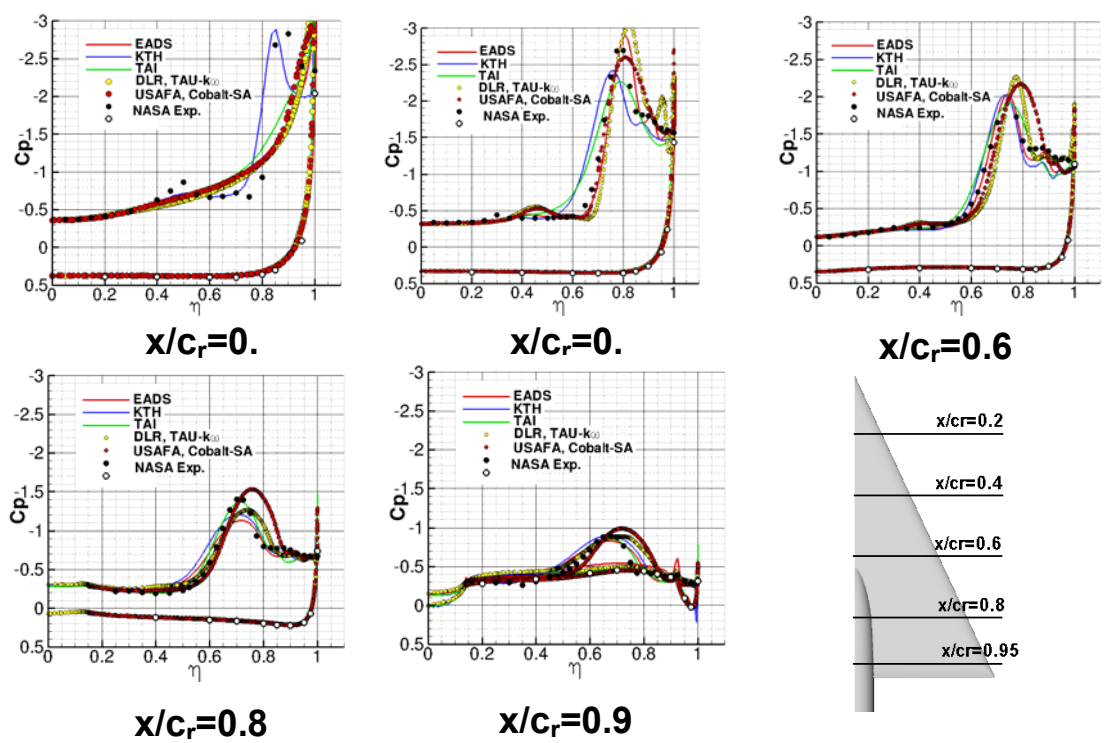

Figure 35-6: Comparison of Calculated Surface Pressures with Experimental Data for the VFE-2 Configuration with Medium Radius Rounded Leading Edges (MRLE) at M = 0.40, α = 18°, Re = 6 x 10^6 [[35-17] and Chapter 34].

35.3.3 Viscous Flow Details

For turbulent flow in solutions of the Reynolds-averaged Navier-Stokes equations a turbulence model has to be applied, which provides additional viscous damping in the boundary layers as well as in the viscous regions of the primary and secondary vortices. The pressure distribution on the upper surface of the wing is very sensitive to correct modelling of the viscous regions of the flow field, and therefore different turbulence models lead to differences in the pressure distributions. Only the correct prediction of the secondary separation line and of the structure of the secondary vortex lead to the right lateral and vertical position of the primary vortex and hence to the correct suction peak in the pressure distribution. Looking into more details of such calculations, the distributions of the total pressure and of the eddy viscosity in the flow field show large differences for different turbulence models.

Within VFE-2 so far all calculations have been carried out for fully turbulent boundary layers and regions with laminar boundary layers have not been taken into account. Attempts have been undertaken to answer the following questions:

- Which turbulence model is best suited for the calculation of vortical flows? Within VFE-2 the experimental part has been treated in detail by HWA, but the numerical part is still open.
- Where is the transition line laminar/turbulent located on the wing? IR and TSP investigations have been carried out within VFE-2, but the evaluations are difficult and they have not yet been finished. Vortical flow calculations for prescribed regions of laminar and turbulent boundary layer have not yet been completed, and the stability analysis of the result for an improvement of the prescription is still open.

Both problems will be discussed subsequently.

35.3.3.1 Flow Field Measurements

In almost all experimental contributions to VFE-2 the time-averaged flow field has been measured using PIV, [35-5], [35-6], [35-7], see Chapters 19, 20, 21. An example is shown in Figure 35-7. The fully developed vortical flow is indicated for both cases, and there are only minor differences concerning the position of the primary vortex relative to the wing.

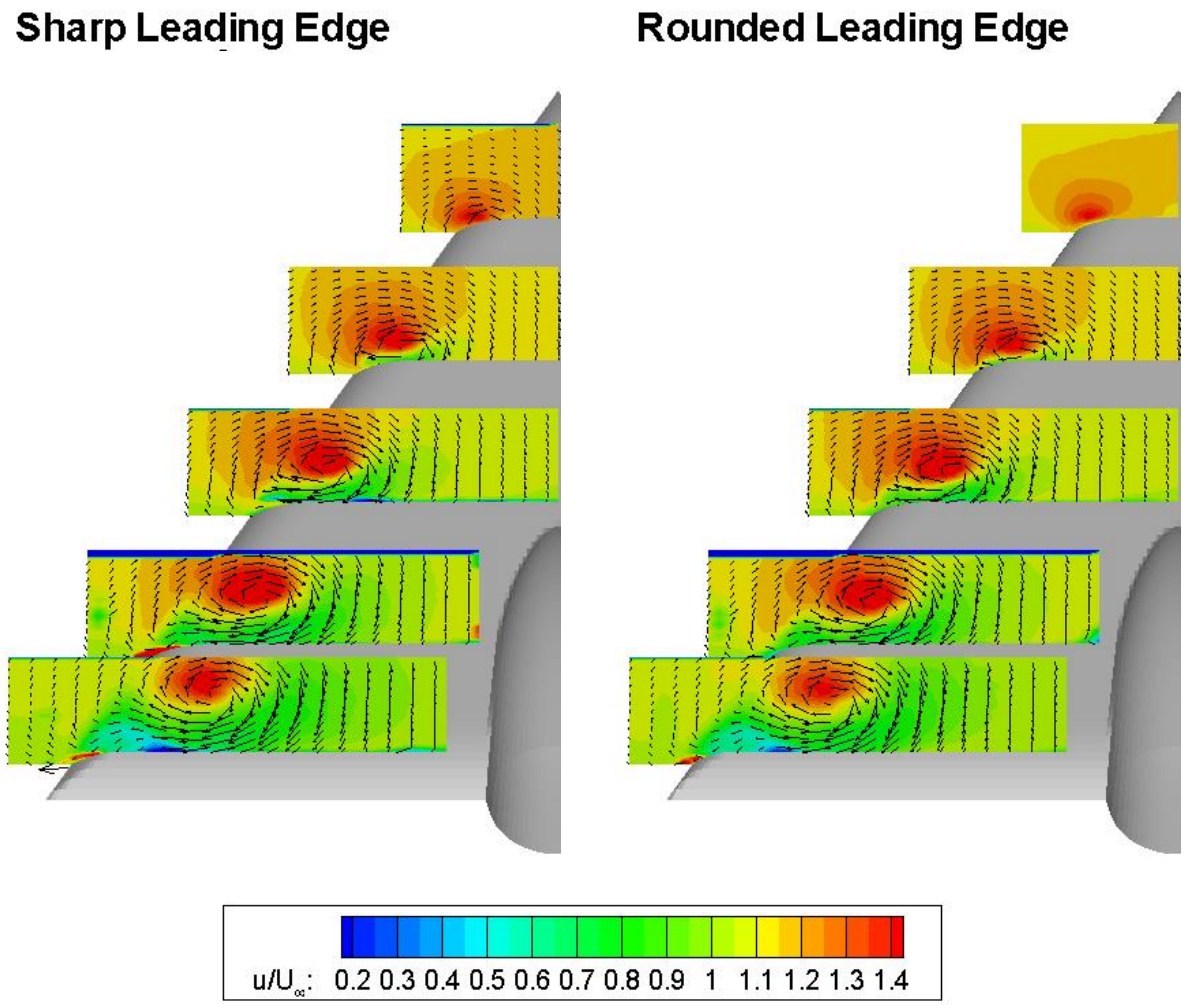

Figure 35-7: Flow Field around the VFE-2 Configuration with Sharp (SLE) and Medium Radius Rounded (MRLE) Leading Edges at M ≈ 0.1, R_{mac} = 1 x 10^6, α = 18°. PIV results for the time-averaged velocity in various cross sections [35-7].

In order to provide experimental data for comparison with numerical flow solutions using various turbulence models, the flow field has been measured by Hot-Wire Anemometry (HWA) at TU Munich [35-7], see Chapter 21, and the complete field of the velocity fluctuations u', v', w' is now available. Again there are only minor differences between the measurements for sharp (SLE) and for medium radius rounded (MRLE) leading edges. Therefore as an example Figure 35-8 shows the measured fluctuations of the u-component of the velocity u_{rms}/U_∞ as well as $\overline{u'w'}/U_\infty^2$ in the cross section plane at x/c = 0.6 for the configuration with sharp leading edges (SLE) only. From the full measured field of the fluctuations u', v', w' the distributions of the turbulent kinetic energy and of the eddy viscosity in the flow field can be determined, and corresponding evaluations of the experiments are still under way.

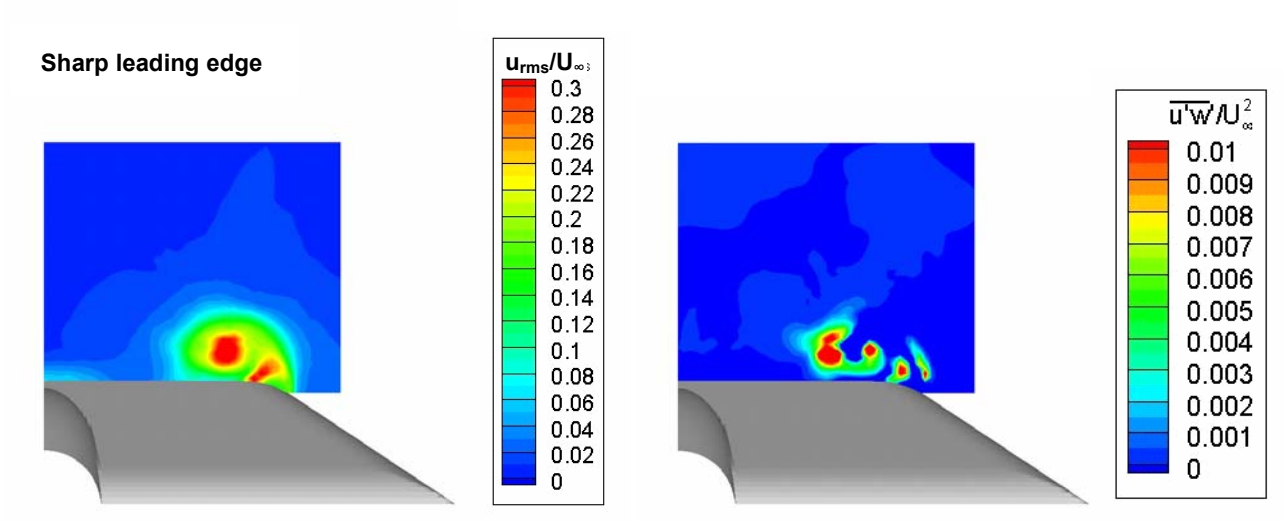

Figure 35-8: Flow Field around the VFE-2 Configuration with Sharp Leading Edges (SLE) at M ≈ 0.1, R_{mac} = 1 x 10^6, α = 18° – HWA Results from TU Munich [35-7] for the Velocity Fluctuations u_{rms}/U_∞ and $\overline{u'w'}/U_\infty^2$ in the Plane at x/c = 0.6.

The unsteadiness of the flow can also be evaluated from these experiments by determining the power spectrum density distribution of any fluctuating flow quantity as function of the frequency at any position in the flow field. An example of this kind is shown in Figure 35-9 for the sharp leading edge (SLE) configuration. In the left-hand graph the distribution of the fluctuations of the u-component of the velocity u_{rms}/U_∞ is given, and the location near the vortex centre is indicated, for which the power spectrum density distribution for the velocity component u/U_∞ is shown on the right-hand side. In this turbulent flow near the vortex centre a large variety of frequencies is present with distinctly high values at low frequencies.

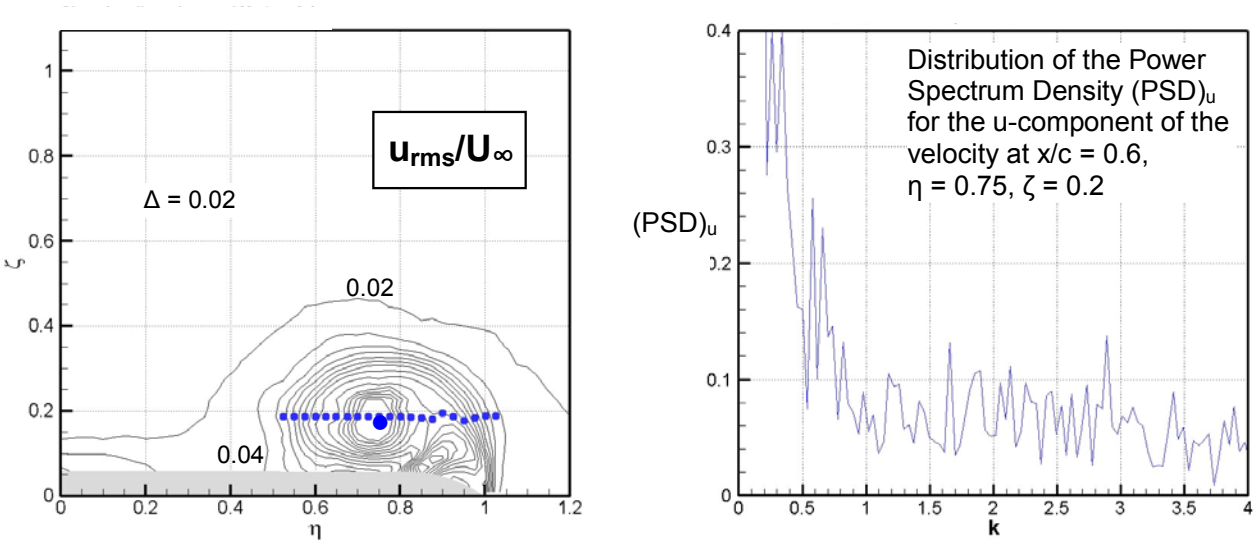

Figure 35-9: Flow Field around the VFE-2 Configuration with Sharp Leading Edges (SLE) at M ≈ 0.1, R_{mac} = 1 x 10^6, α = 18° – Power Spectrum Density $(PSD)_u$ for the u-Component of the Velocity as Function of the Reduced Frequency k at x/c = 0.6, η = 0.75, ζ = 0.2 According to HWA at TU Munich [35-7].

In order to find the best suited turbulence model for vortical flow simulations the results of these unsteady flow field measurements will be used for comparisons with numerical calculations. Unfortunately, however, it was only possible to carry out these experiments for incompressible flow ($M \approx 0.1$) and for a very low Reynolds number ($R_{mac} = 1 \times 10^6$), and this causes serious problems on the numerical side, since the convergence rate of the various computer codes is very low. Up to now no comparisons have been performed, and the numerical part of this task is still open.

35.3.3.2 Laminar/Turbulent Transition

The laminar/turbulent transition within the upper surface boundary layer of a delta wing is poorly known even for the simplest case of a sharp leading edge configuration. Following the flow separation at the leading edge the vortical flow reattaches on the upper surface of the wing. This is demonstrated in Figure 35-10 by oilflow patterns taken long ago by the author on the upper surface of the VFE-1 delta wing configuration [35-3] at $M \approx 0.1$, $\alpha = 10°$ for two different Reynolds numbers. The reattachment line (a) is clearly indicated for both Reynolds numbers. Underneath the primary vortex the flow is directed outboard and an acceleration takes place until the surface pressure minimum is reached. Further outboard the pressure increase towards the leading edge leads to a secondary separation and to the formation of a secondary vortex underneath the primary vortex. At very low Reynolds numbers the reattached boundary layer flow is laminar everywhere (see $R_{mac} = 0.42 \times 10^6$), and this leads to an early secondary separation (sl) in a quite large distance from the leading edge. At a higher Reynolds number, however, in the rear part of the wing transition laminar/turbulent may occur due to increased distance from the apex and underneath the primary vortex the adverse pressure gradient towards the leading edge causes also transition laminar/turbulent prior to the secondary separation. Since turbulent boundary layers stay longer attached, the secondary separation line is then shifted towards the leading edge if the separating boundary layer has undergone transition. This phenomenon can be recognized in Figure 35-10 for $R_{mac} = 0.93 \times 10^6$. The kink in the secondary separation line is located at $x/c_r \approx 0.3$. For $x/c_r \leq 0.3$ a laminar boundary layer separates, whereas for $x/c_r \geq 0.3$ the separating boundary layer is turbulent.

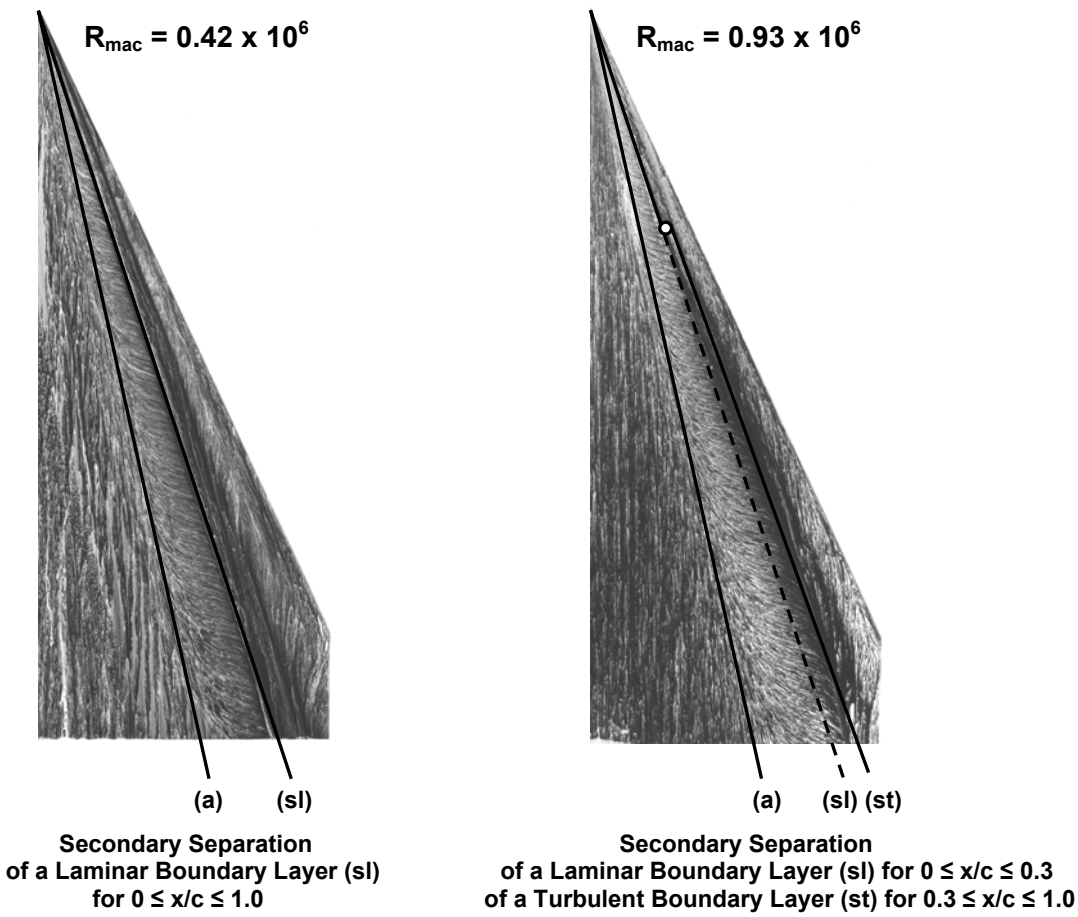

Figure 35-10: Surface Oilflow Patterns on the Upper Surface of the Sharp-Edged VFE-1 Cropped Delta Wing (Leading Edge Sweep Λ = 65°) at M = 0.12, α = 10° for Different Reynolds Numbers.

On the wing surface there exists a transition line, which connects all transition points and which starts at the kink in the separation line. It is important to note that this transition line is not known. Up to now no systematic investigations have been carried out to determine the regions of laminar and of turbulent flow on a sharp edged delta wing. If a method would come up to predict these regions, we would not be able to validate it due to lack of experimental data. On the other hand CFD calculations are presently carried out either for fully laminar or for fully turbulent flow. For very high Reynolds numbers the laminar flow part near the apex of the wing is very small, and calculations for fully turbulent flow are justified in this case. For moderate and low Reynolds numbers, however, in CFD calculations the laminar front part should be taken into account properly and this could be done using an experimentally determined transition location.

For wings with rounded leading edges the primary flow separation is no longer enforced by the leading edge shape. The primary flow separation takes place somewhere in the leading edge region, but the separation line is no longer fixed to the leading edge. Its position depends on the status of the lower surface boundary layer being either laminar or turbulent. This means that the lower surface boundary layer status at the leading edge effects the formation of the primary vortex on the upper surface of the wing. Underneath the primary vortices the upper surface boundary layer formation virtually takes place according to the principles described so far for the sharp leading edge case.

Within VFE-2 attempts have been undertaken to determine the laminar/turbulent transition experimentally, see Chapters 19 and 23. If Temperature Sensitive Paint (TSP) and Infrared Techniques (IR) are used, the position of the temperature jump at transition has to be determined. Unfortunately underneath the primary vortex a considerable temperature distribution is generated on the wing surface due to compressibility effects even for nearly incompressible flow, which has to be separated from the artificially generated temperature distribution caused by the heated or cooled wind tunnel model. Evaluations of this kind are complicated and final results of these experiments are not yet available.

On the numerical side calculations have been started within VFE-2 to produce a solution for the RANS equations for a prescribed distribution of laminar and turbulent boundary layer regions on the wing, which could be chosen according to available experimental results. On the basis of a converged numerical solution a point by point stability analysis should then justify or modify the prescribed transition line on the wing. Unfortunately these investigations could not be finished within the RTO phase of VFE-2.

At the end of the RTO phase of VFE-2 the experimental and the numerical determination of the laminar/ turbulent transition are still open and further investigations on this subject are necessary. The existing attempts will be continued and new investigations are encouraged to be carried out within the subsequent open phase of VFE-2 in the years to come.

35.4 FULLY SEPARATED FLOW WITH VORTEX BREAKDOWN

In this section the results for the VFE-2 configuration at *angle of attack* $\alpha = 23°$ are discussed. In this case the flow is fully separated and vortex breakdown takes place in the rear part of the wing. Today it is common understanding that the flow past slender delta wings at large angles of attack becomes unsteady even for fixed wings. This means that for large angles of attack and steady boundary conditions only unsteady solutions of the governing equations do exist. The spiral-type vortex breakdown is well predicted by numerical solutions of the Navier-Stokes equations [[35-17] and Chapters 25 and 34], see Figure 35-11. The instantaneous vortex axis spirals in space against the sense of rotation of the primary vortex and this spiral turns around with respect to time in the sense of rotation of the primary vortex, and in the centre of the spiralling motion a region of reversed flow is present. Correspondingly all quantities of the flow field show oscillations.

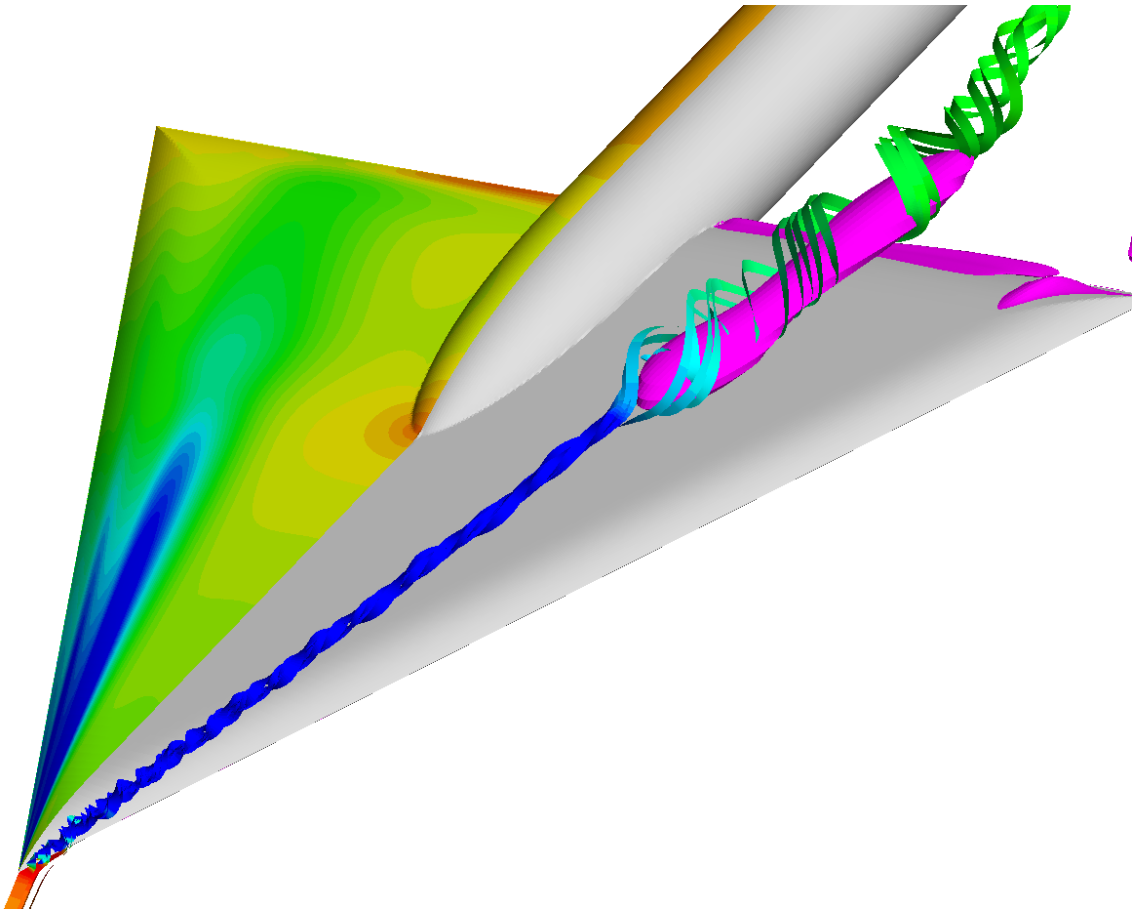

Figure 35-11: Numerical Simulation of the Flow around the VFE-2 Configuration with Sharp Leading Edge (SLE) for M = 0.4, R_{mac} = 6 x 10^6, α = 23° [[35-17] and Chapters 25 and 34]. Surface pressure distribution (left) and flow field (right).

35.4.1 Subsonic Flow Investigations

35.4.1.1 Surface Pressure Fluctuations

In new experiments on the VFE-2 configuration unsteady pressure distribution measurements have been carried out [[35-7] and Chapter 21] in order to provide data on the oscillations including the governing frequencies for comparison with numerical results. As an example, for the configuration with medium radius rounded leading edges (MRLE) Figure 35-12 shows the surface pressure fluctuations $(C_p)_{rms}$ in four cross sections on the wing, and for a certain station in each of these distributions the amplitude spectrum $(SD)_{cp}$ of the pressure fluctuations as a function of the reduced frequency $k = f\bar{c}/U_\infty$ is given. The high values of the fluctuations around $k \approx 1.3$ in the last section are caused by the spiral motion of vortex breakdown.

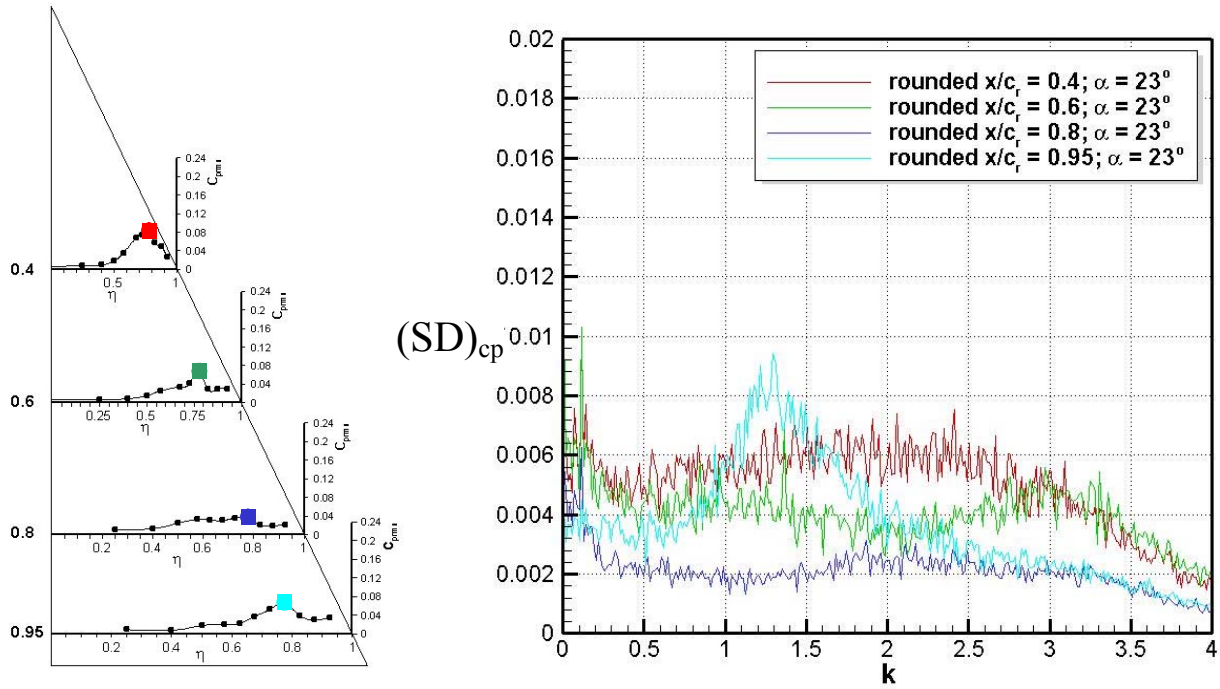

Figure 35-12: Flow Field around the VFE-2 Configuration with Medium Radius Rounded Leading Edges (MRLE) at M = 0.14, R_{mac} = 2 x 10^6, α = 23°. Surface pressure fluctuations $(C_p)_{rms}$ and spectrum density $(SD)_{cp}$ for certain stations in four cross sections according to the measurements at TU Munich [[35-7] and Chapter 21].

35.4.1.2 Unsteady Flow Field

Flow field measurement in various cross sections have also been carried out for α = 23° at TU Munich [[35-7] and Chapter 21]. In these cross sections the time-averaged flow field has been measured by means of PIV investigations and the complete unsteady flow field has been determined using the HWA technique. For the configuration with medium radius rounded leading edge (MRLE) Figure 35-13 shows the unsteadiness of the flow field with vortex breakdown in the cross section at x/c = 0.8. The annular form of the area with high fluctuations is typical for the spiral mode of vortex breakdown, and further analysis of these data will lead to experimental results for the frequency of the spiral mode of vortex breakdown. Evaluations of this kind are presently under way.

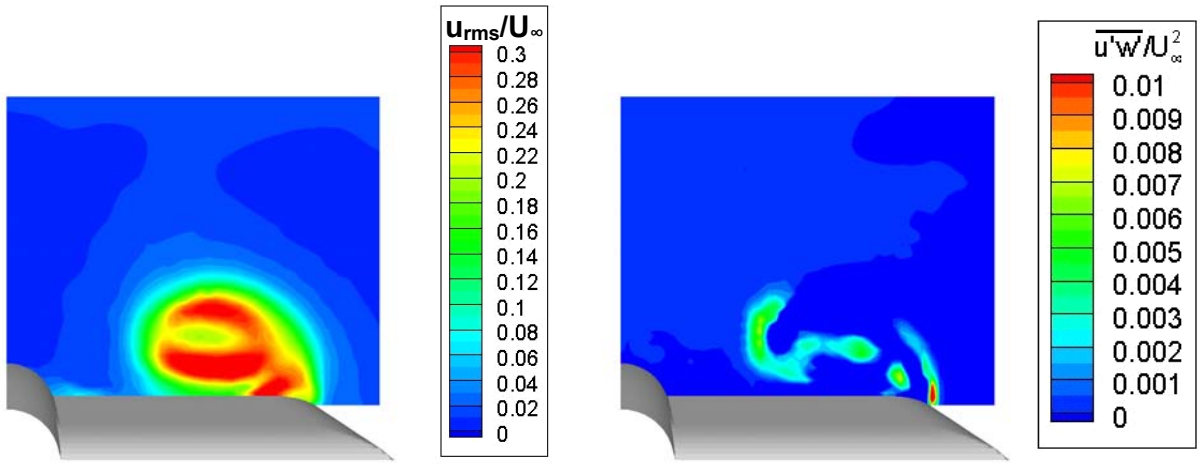

Figure 35-13: Flow Field around the VFE-2 Configuration with Medium Radius Rounded Leading Edges (MRLE) at M ≈ 0.1, R_{mac} = 1 x 10^6, α = 23°. HWA results from TU Munich [[35-7] and Chapter 21] for the velocity fluctuations u_{rms}/U_∞ and $\overline{u'w'}/U_\infty^2$ in the cross section at x/c = 0.8.

Unfortunately these measurements could only be carried out for incompressible flow (M ≈ 0.1) and for very low Reynolds numbers (R_{mac} = 1 x 10^6). In comparisons with flow simulations these conditions cause serious problems on the numerical side, since the convergence rate of the various computer codes is very low. Up to now no comparisons have been performed, and the numerical part of this task is still open.

35.4.1.3 Time-Averaged Surface Pressure Distributions

For comparison with numerical results experimental surface pressure distribution data are available from the NASA measurements [35-1]. Since the vortical flow with vortex breakdown is unsteady, numerical simulations have to be carried out time-accurate, but in the subsequent comparison with experimental data again time-averaged quantities are used. A comparison of this kind is shown in Figure 35-14 for the sharp leading edge (SLE) VFE-2 configuration [[35-17] and Chapter 34]. All numerical simulations predict the onset of vortex breakdown at about x/c_r = 0.6, whereas in the experiments vortex breakdown occurs more downstream. In addition the gradient of the reduction of suction towards the trailing edge is different for the shown numerical solutions. A more detailed comparison of the numerical solutions with the experimental data is presented in Figure 35-15. In the two most upstream cross sections the numerical solutions match the main flow features quite well and the differences are found in the levels of the main suction peak and in the details of the secondary vortex region. However, for $x/c_r \geq 0.6$ some discrepancies are visible. All numerical solutions show a less compact and smeared out vortex as compared to the experimental data.

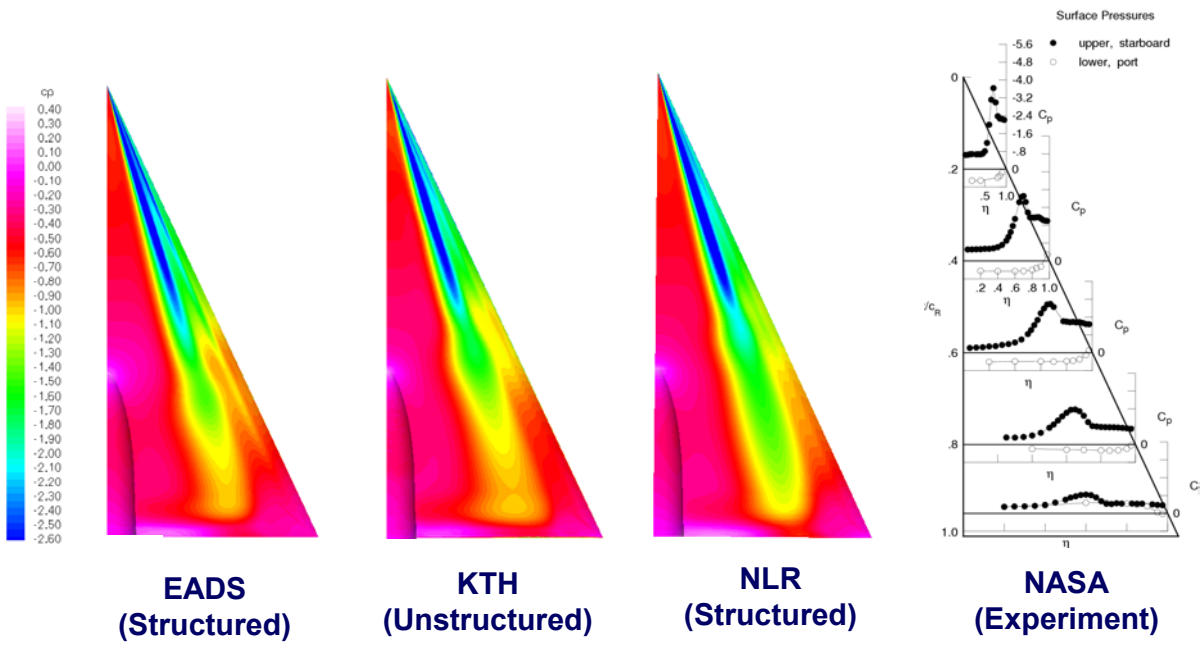

Figure 35-14: Surface Pressure Distribution on the VFE-2 Configuration with Sharp Leading Edges (SLE) at M = 0.40, α = 23°, Re = 6 x 10^6 [[35-17] and Chapter 34].

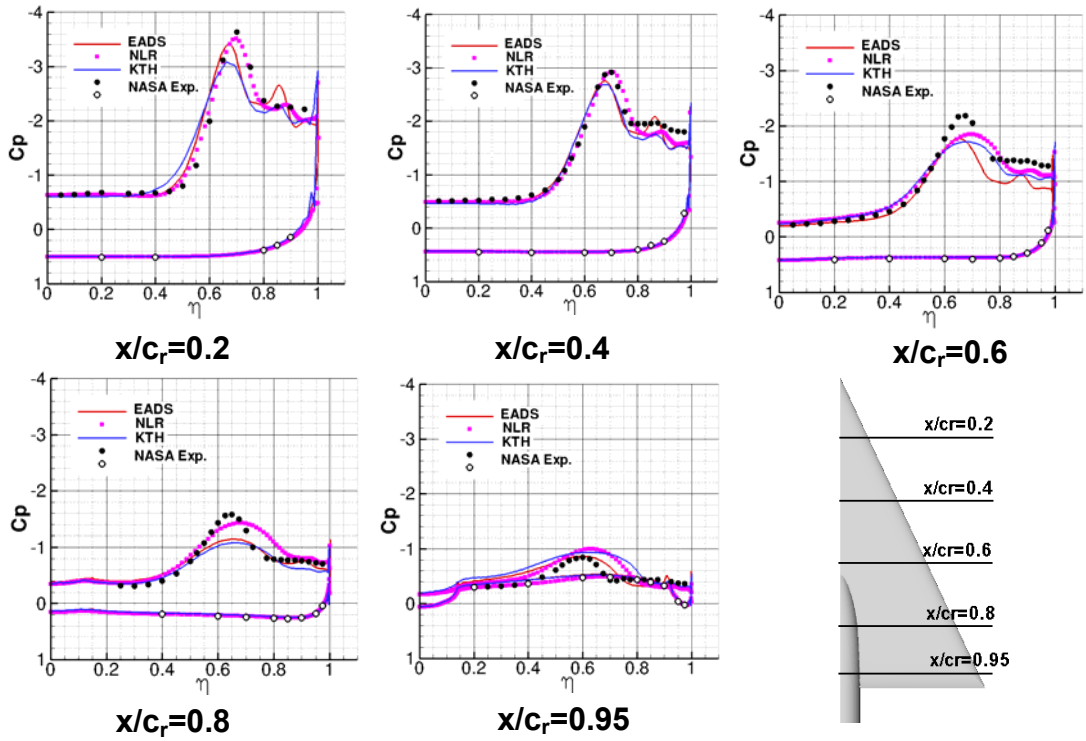

Figure 35-15: Comparison of Calculated Surface Pressures with Experimental Data for the VFE-2 Configuration with Medium Radius Rounded Leading Edges (MRLE) at M = 0.40, α = 23°, Re = 6 x 10^6 [[35-17] and Chapter 34].

35.4.2 Transonic Flow Investigations

35.4.2.1 Experimental Results

For high angles of attack the wind tunnel investigations showed a large effect of Mach number on the vortex breakdown position and hence on the pressure distribution. This is demonstrated in Figure 35-16 for the VFE-2 configuration at $\alpha = 25°$, $R_{mac} = 2 \times 10^6$ and two different Mach numbers. In both cases only moderate differences exist between the results for sharp and blunt leading edges. At the lower Mach number M = 0.4 (left-hand part) no supersonic zones and no shock waves do exist for $\alpha = 25°$. At this angle of attack vortex breakdown would certainly be ahead of x/c = 0.8, although the precise breakdown location is in general difficult to discern from subcritical surface pressure information. At constant angle of attack and with the increase to a transonic Mach number, however, a distinct change of the pressure distribution on the wing can be taken from the results for M = 0.8 (right-hand part). At this transonic Mach number a local supersonic zone with a shock wave is formed in the vicinity of the sting mount. The adverse pressure jump in the shock wave causes additional unsteadiness in the vortical flow field, and most likely shifts vortex breakdown upstream.

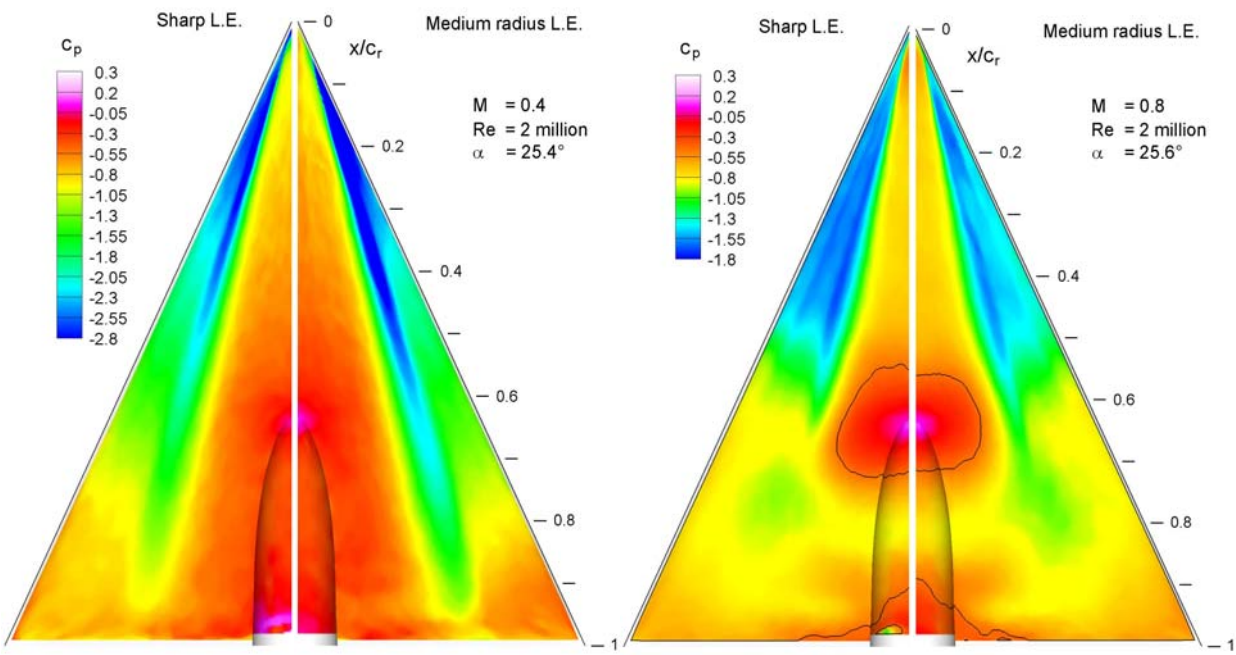

Figure 35-16: Pressure Distributions on the VFE-2 Configuration with Sharp and Medium Radius Rounded Leading Edges (MRLE) at $R_{mac} = 2 \times 10^6$ and $\alpha = 25°$ for Two Mach Numbers According to the PSP Experiments at DLR Goettingen [[35-5] and Chapter 19]. The black line indicates the sonic pressure coefficient.

35.4.2.2 Numerical Results

The surface pressure distributions according to four different numerical solutions together with the experimental data [35-1] are shown in Figure 35-17. There are three very similar solutions by EADS, NLR and KTH, see Chapters 25, 27 and 30. The TAI solution, see Chapter 28, however, is distinctly different, but it is more similar to the experimental data. In the front part at $x/c_r = 0.2$ and $x/c_r = 0.4$ the numerical results of EADS, NLR and KTH are identical and they match the experimental data, whereas in the TAI solution the

initial primary vortex is obviously weaker. At $x/c_r = 0.6$ neither in the experiments nor in the TAI solution a shock has been passed in the flow field, and therefore the TAI solution nicely coincides with the experimental data. The other three solutions are again very similar and they all show the pressure jump due to the shock already at $x/c_r \approx 0.5$. Therefore these solutions do not match the experimental data at $x/c_r = 0.6$, but they still indicate some vortical structure there. In the cross sections $x/c_r = 0.8$ and $x/c_r = 0.95$ the solutions of EADS, NLR, and KTH all show a dead water type pressure distribution without any vortical structure, whereas the TAI solution indicates a vortical structure, which fits the experimental data very well.

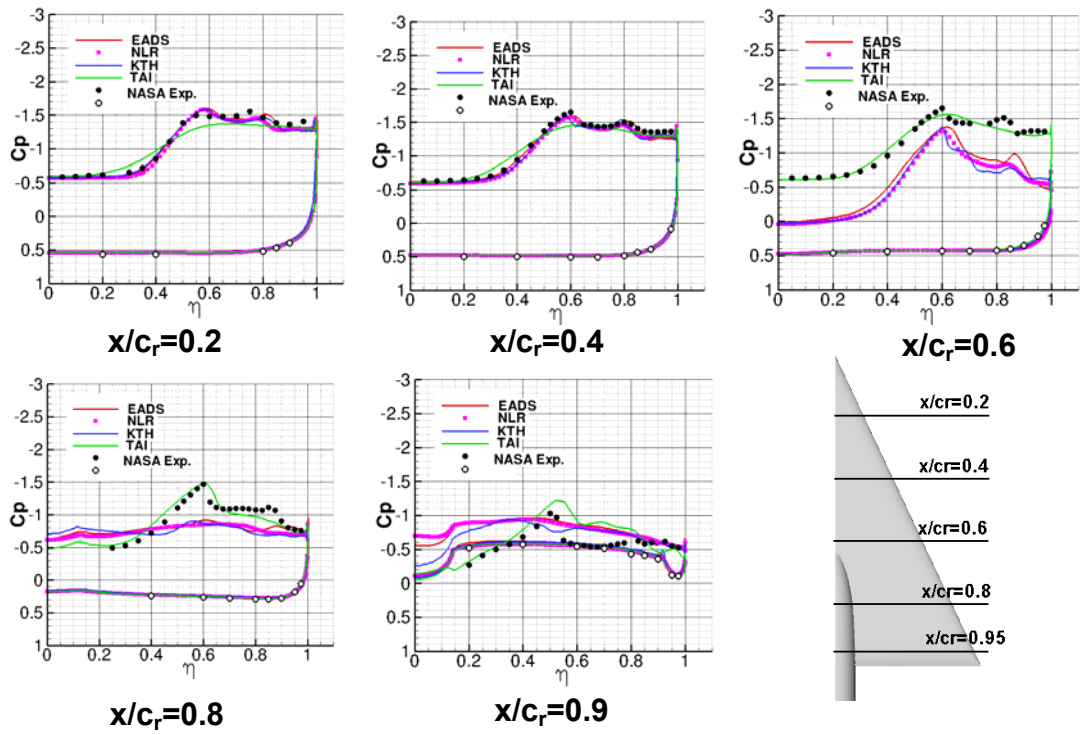

Figure 35-17: Comparison of Calculated Surface Pressures with Experimental Data for the VFE-2 Configuration with Sharp Leading Edges (SLE) at M = 0.85, α = 23°, Re = 6 x 10^6 [[35-17] and Chapter 34].

A closer look into the surface pressure distributions is shown in Figure 35-18. In the EADS solution, which is representative also for the two other solutions, a strong shock occurs at $x/c_r \approx 0.5$, a dead water type flow is indicated downstream of the shock, and a terminating shock is present at the inner part of the wing. In addition a very significant secondary vortex turns out, which also interacts with the shock. The TAI solution shows a much weaker and more smeared out single vortex in the forward part of the wing, which produces obviously a weaker and more downstream positioned shock. The suction peak is only slightly reduced across this shock. More downstream, at $x/c_r \approx 0.8$, a second weak shock wave builds up from the wing leading edge towards the suction peak. When reaching the suction peak, this shock wave turns at 90° angle and becomes a weak cross flow shock, which finally merges with the terminating shock close to the trailing edge. This result for the shock formation can also be concluded from the experimental pressure distribution, since the measurements at $x/c_r = 0.8$ and $x/c_r = 0.95$ also give an indication of a weak cross flow shock.

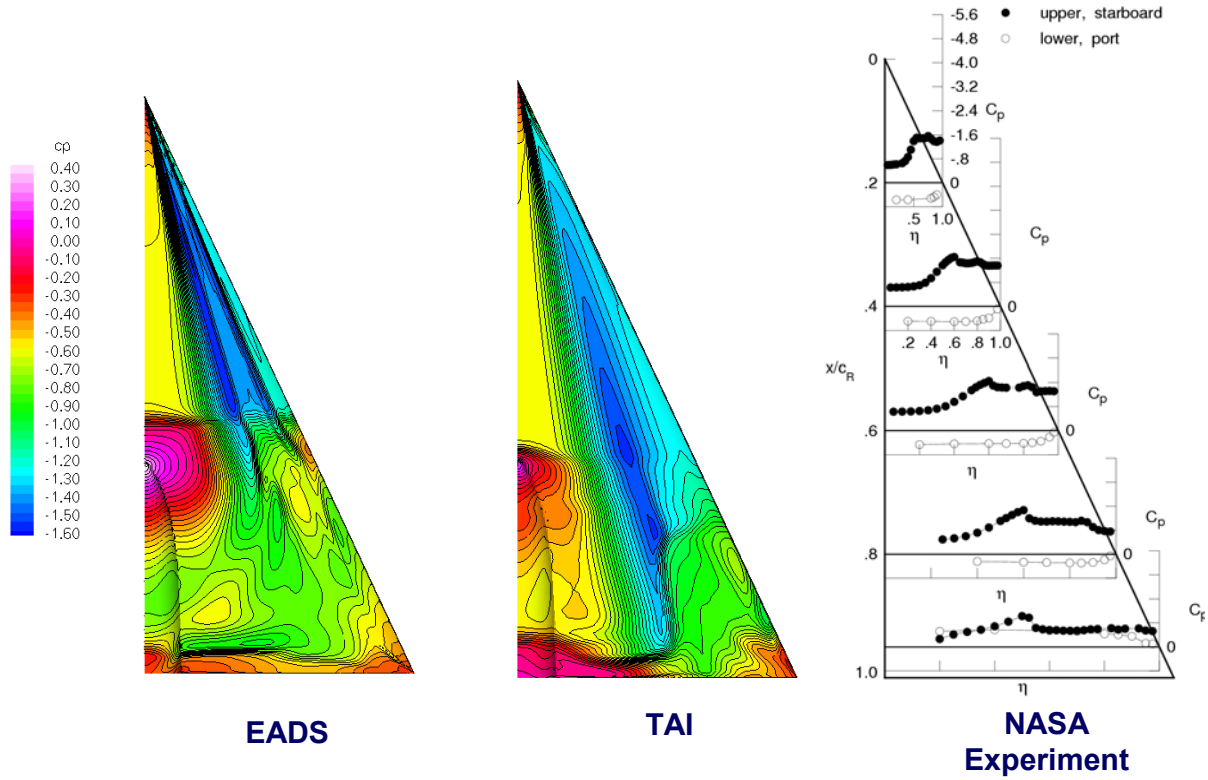

Figure 35-18: Surface Pressure Maps on the VFE-2 Configuration with Sharp Leading Edges (SLE) at M = 0.85, α = 23°, Re = 6 x 10^6 [[35-17] and Chapter 34].

In transonic flow the upstream shift of the vortex breakdown position is caused by shock waves. Within VFE-2 this phenomenon has been studied intensively by joint numerical investigations [35-13], see Chapter 29. For the VFE-2 configuration the sting mount might be regarded to be responsible for the occurrence of this shock, but numerical investigations at KTH, see Chapter 30, have indicated that such shocks occur also for the clean wing without a sting mount and furthermore in transonic flow an unsteady shock system may be present. The numerical results according to Figure 35-18 show shock shapes, which have never seen before in experimental results. Therefore new measurements should be carried out related to shock formation and vortex breakdown onset as well as concerning their mutual interference. On the other hand the available numerical tools should be checked for the correct prediction of the shock shape and its position in the vortical flow field, since the present investigations have shown that numerical surface pressure distributions fit experimental data only if the shocks are covered properly.

35.5 PARTLY SEPARATED VORTICAL FLOW

In this section the results for the VFE-2 medium radius rounded leading edge (MRLE) configuration at *angle of attack α = 13°* are discussed. In this case partly separated flow is present on the upper surface of the wing [35-1] as sketched in Figure 35-19 according to [35-17]. This is the most challenging flow situation both experimentally and numerically. A semi-empirical attempt [35-10] for the prediction of the distance x_V of the separation onset has been carried out, see Chapter 33, but the more detailed findings within VFE-2 and the remaining problems are discussed subsequently.

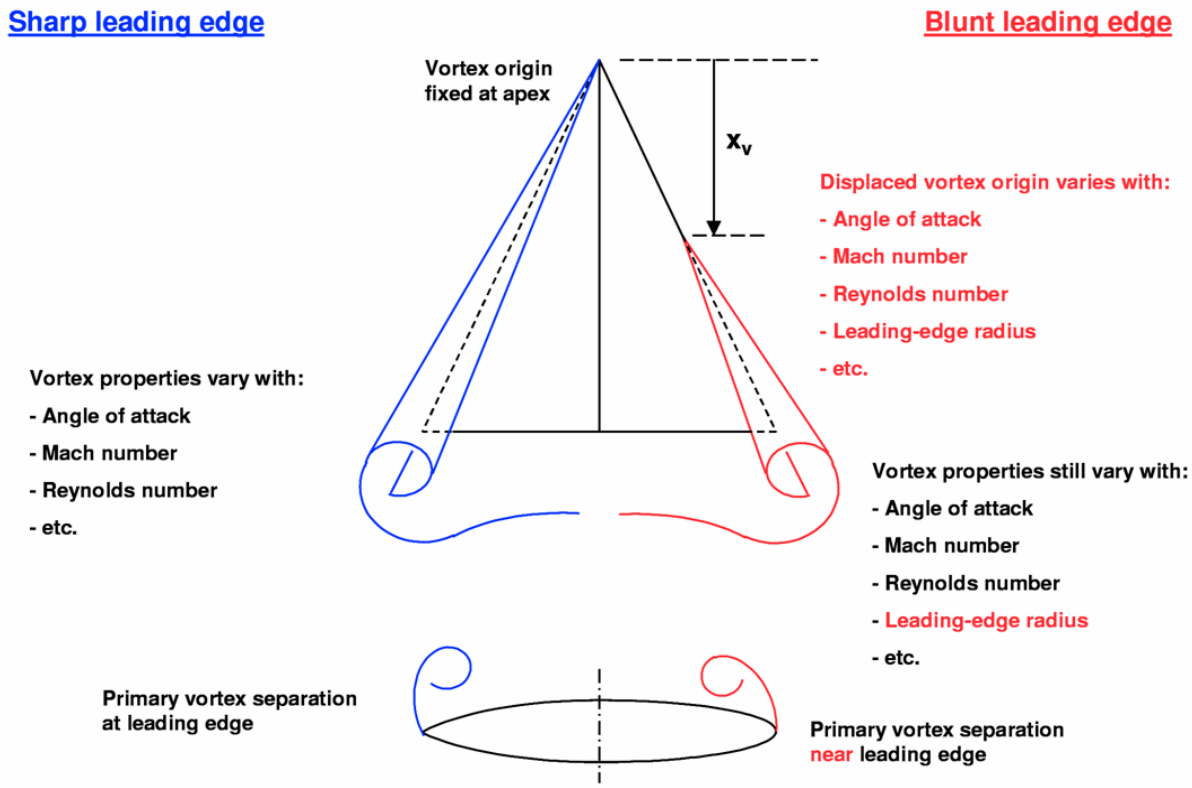

Figure 35-19: Comparison of Vortical Flow Features for Sharp and Blunt Leading Edge Delta Wings According to [35-1], taken from [35-17].

35.5.1 Overall Forces and Moments

The effect of leading-edge bluntness on the normal force and pitching moment coefficients for the VFE-2 configuration is presented in Figure 35-20 from measurements taken in the NASA Langley NTF at a Mach number of 0.4 and a Reynolds number of 6 million. At low angles of attack both wings develop the same normal force. The blunt leading edge wing has attached flow at these conditions, and any leading-edge vortex separation effects for the sharp-edged wing are very small at these low angles of attack. Over the rest of the angle of attack range investigated the blunt leading edge wing develops less normal force than the sharp-edged wing. The blunt leading edge weakens the leading edge vortex resulting in reduced vortex-induced normal force. Pitching moments show the blunt-edged wing has a more forward center of pressure, compared to the sharp-edged wing, over the range of conditions investigated. The vortex flow physics associated with these effects may be taken from the following discussions.

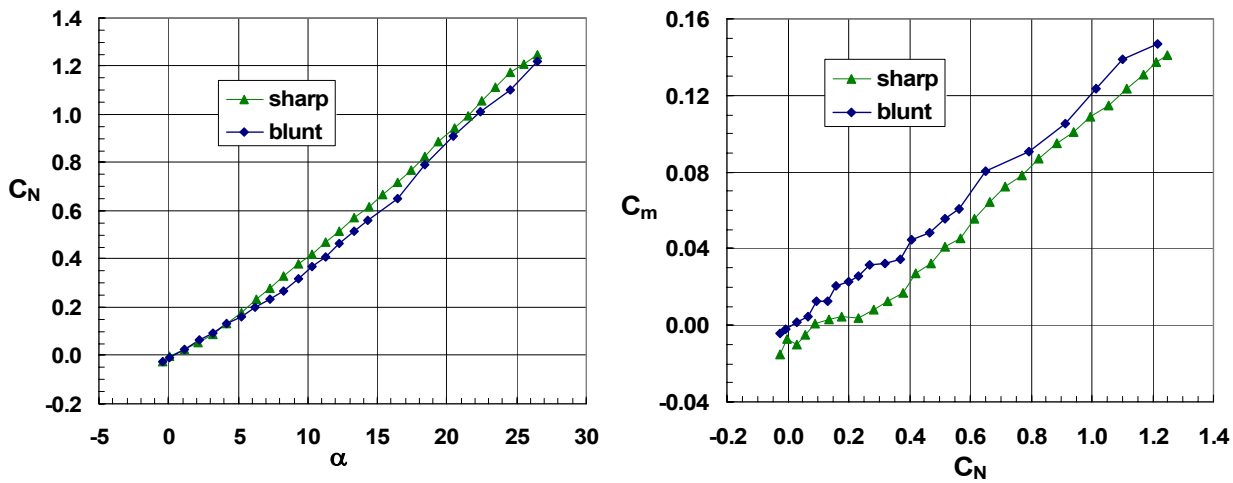

Figure 35-20: Effect of Bluntness on Experimental Normal Force and Pitching Moment Coefficients for the VFE-2 Configuration with Sharp (SLE) and Medium Radius Rounded Leading Edges (MRLE) at M = 0.4, R_{mac} = 6 x 10^6. Results from NASA Langley NTF [35-1].

35.5.2 Pressure Distributions

The experimental pressure distribution on the VFE-2 configuration with medium radius rounded leading edges (MRLE) at Mach number M = 0.4 and Reynolds number R_{mac} = 3 million at an angle of attack α = 13° [35-5], see Chapter 19, is shown in Figure 35-21. On the left-hand side the pressure distributions according to PSI experiments from pressure tabs are shown. In the region of attached flow near the apex of the wing high suction occurs at the leading edge. Further downstream an inner suction peak develops followed by an even higher outer suction peak, which replaces the original leading edge suction. Towards the trailing edge of the wing the outer suction peak is still maintained, whereas the inner suction peak reduces more and more and finally disappears. The PSP results on the right-hand side show these features in the same way. The full view of the pressure distribution on the configuration is given in the coloured figure in the centre of Figure 35-21. It shows the onset of the strong outer suction peak to be located at about x/c_r = 0.45 and undoubtedly this suction peak is related to the primary vortex of the separated flow. In order to clarify the flow structures related to the inner suction peak, 3D PIV investigation have been carried out. Figure 35-22 shows the result for the flow field in various cross-sectional planes [35-5], see Chapter 19, in comparison with the numerical result. The surface pressure distribution from the PSP investigations according to Figure 35-21 is repeated in colours for the right half of the wing in the left-hand figure. The outer suction peak underneath the primary vortex is marked by the green area and the one underneath a second, inner vortex can be identified by a yellow band. Two vortices with the same sense of rotation are clearly indicated in the rear part of the wing. Around x/c_r = 0.7 the size of both vortices is about the same as predicted by the CFD results shown in the right-hand figure. More downstream the outer vortex becomes the stronger one, whereas the inner vortex decays. The experimental results are in excellent agreement with the numerical findings [35-11], see Chapter 25, as shown in the right-hand figure.

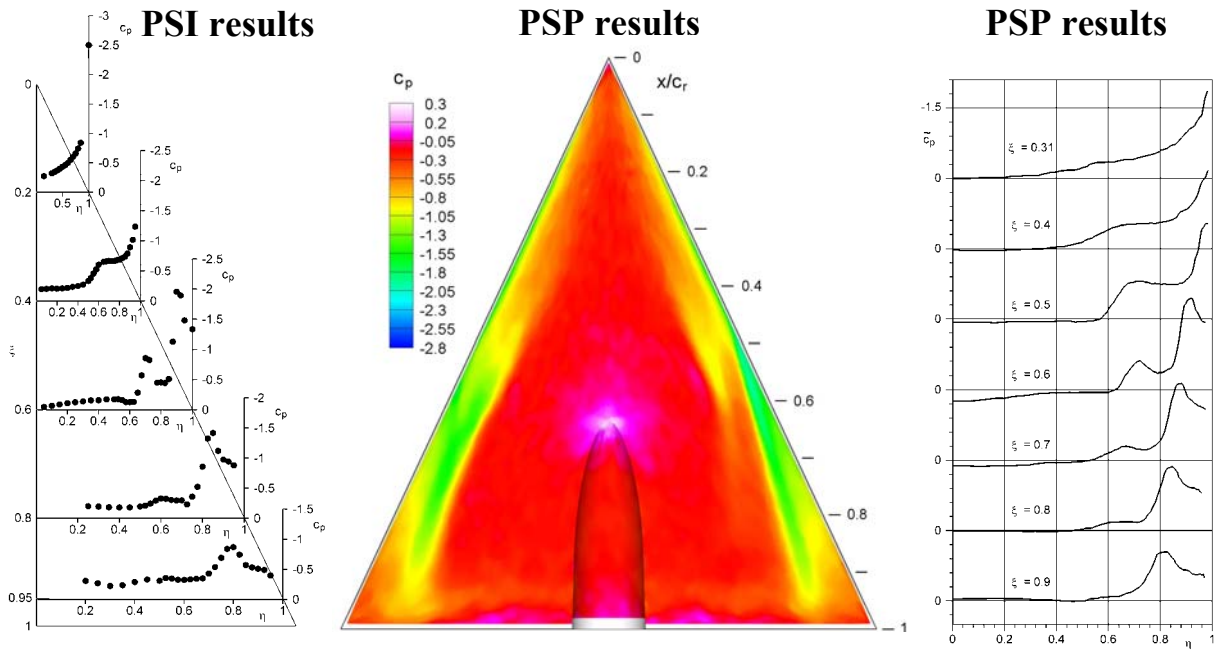

Figure 35-21: Experimental Pressure Distribution on the VFE-2 Configuration with Medium Radius Rounded Leading Edges (MRLE) for M = 0.4, R_{mac} = 3 x 10^6, α = 13° [[35-5] and Chapter 19].

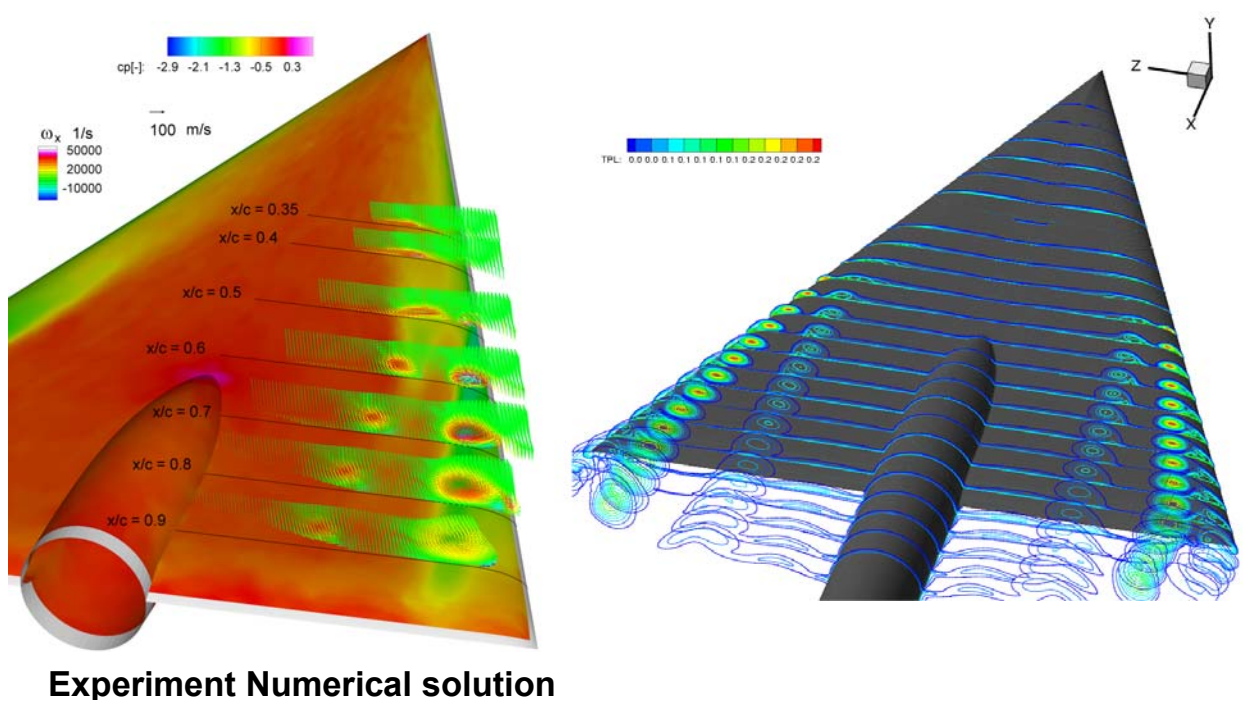

Figure 35-22: Pressure (Surface Color), Velocity (Vectors) and Vorticity (Vector Color) Distributions above the VFE-2 Configuration with Medium Radius Rounded Leading Edges (MRLE) for M = 0.4, R_{mac} = 3 x 10^6, α = 13°. Comparison of the PSP and PIV measurements (left) with the numerical solution (right).

After the encouraging first numerical results [35-11], see Chapter 25, almost all available CFD codes have been applied to the experimentally documented flow case M = 0.4, $R_{mac} = 3 \times 10^6$, α = 13°. The result for the comparison of different numerical pressure maps with the experimental result of DLR [35-17], see Chapter 34, is shown in Figure 35-23. The dashed horizontal line indicates the onset of the main primary separation in the experiment. The prediction of this vortex onset is the main difference between the various numerical solutions. The EADS-solution [35-11] has this onset point slightly behind, but very close to the experimental onset point. The other solutions show a slightly more upstream position (DLR [35-16], TAI [35-12], and USAFA [35-14]) or a considerable more upstream position (KTH [35-15]) of the onset point. Except for the TAI-solution all other results show the footprint of the inner vortex. Possibly the TAI-grid with 2 million grid points is not fine enough to resolve this flow feature. As can also be seen, none of the solutions exactly matches the experimental surface pressure pattern.

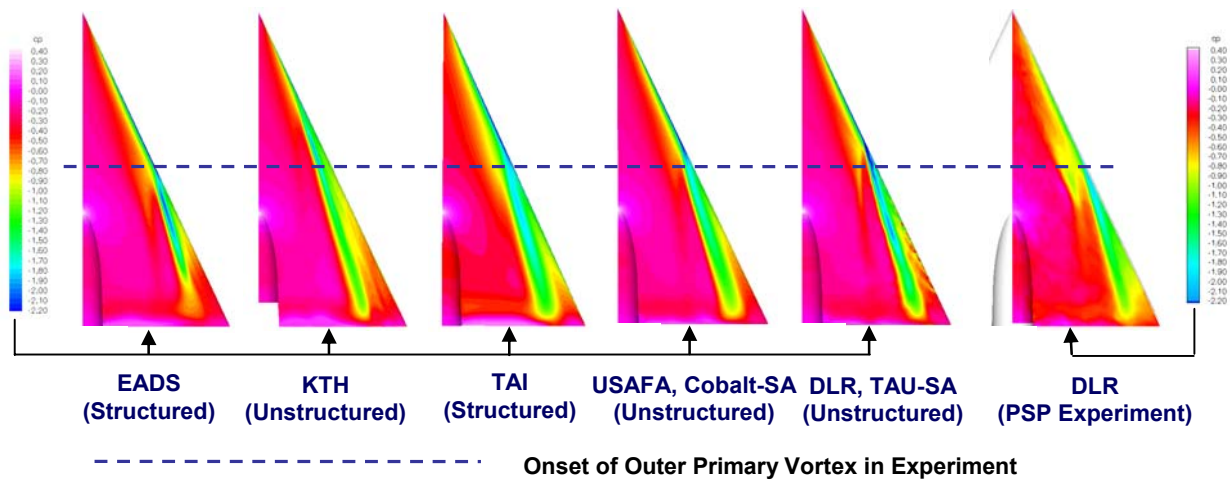

Figure 35-23: Surface Pressure Distribution on the VFE-2 Configuration with Medium Radius Leading Edges (MRLE) at M = 0.40, α = 13°, Re = 3 x 10^6 [[35-17] and Chapter 34].

A more detailed comparison of the surface pressure distribution is given in Figure 35-24. At the first shown cross section at $x/c_r = 0.2$, where no leading edge separation occurs, all numerical pressure distributions are identical and agree well with the experimental data. At $x/c_r = 0.4$ the same applies for four of the five numerical pressure distributions, but the KTH solution [35-15] already shows the formation of a primary vortex. In addition the experimental pressure distribution in this section indicates the beginning of an inner vortex formation, and this effect can also slightly be seen in the KTH solution. At $x/c_r = 0.6$, all solutions as well as the experimental data clearly show a primary vortex, but there are differences in the position and the magnitude of the corresponding suction peak. These differences can be related to the onset of the primary leading edge separation. The more upstream this separation is prescribed, the more inboard located is the suction peak due to the primary vortex. The experimental data also show very clearly the effect of the second, inner vortex. Its foot print is not present in the TAI solution [35-12] and it is hard to identify in the KTH solution [35-15], but the other three solutions [35-12], [35-14], [35-16] clearly indicate the effect of the inner vortex. The EADS solution [35-11] shows this second peak at the correct spanwise position. In the DLR [35-16] and USAFA [35-14] solutions the outer primary vortex is already more inboard as compared with the experiment, and consequently the inner suction peak is also more inboard located. However, in all these three solutions the inner vortex is too weak in comparison with the experiment. In the last cross sections at $x/c_r = 0.8$ and 0.95 the various results are very similar. The more upstream the leading edge separation has

been predicted, the more inboard located is the outer primary vortex. The footprint of the inner vortex has become very weak, and those solutions, which showed the inner vortex in the cross section at $x/c_r = 0.6$ also show the decrease of this vortex.

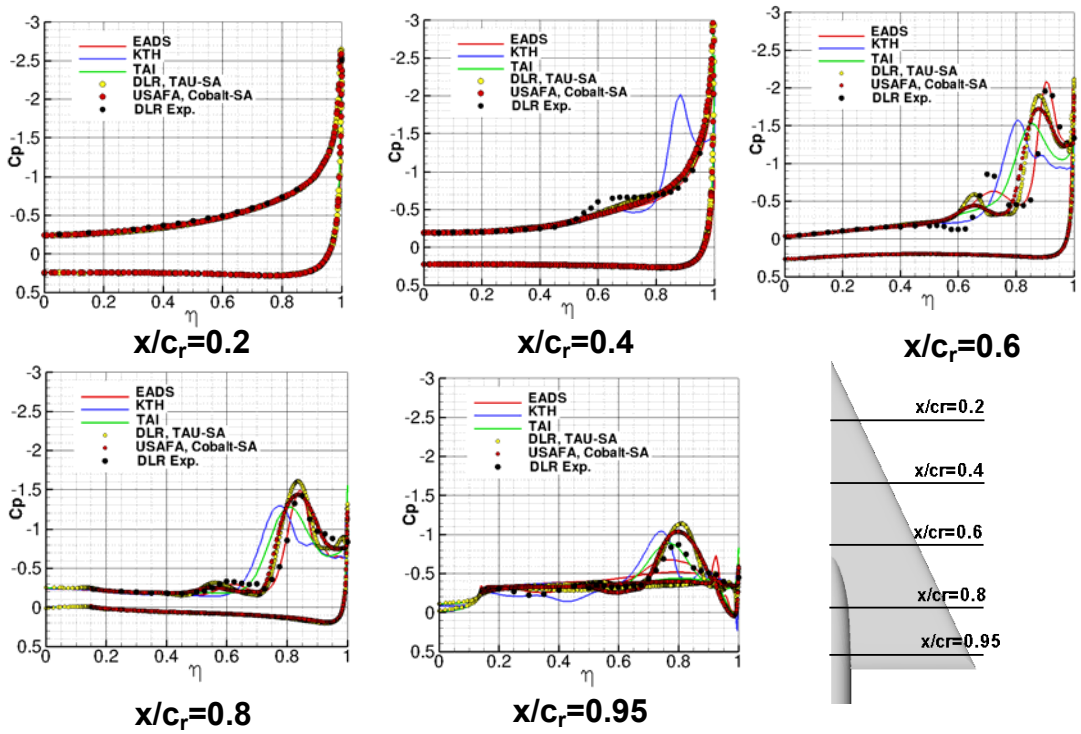

Figure 35-24: Comparison of Calculated Surface Pressures with Experimental Data for the VFE-2 Configuration with Medium Radius Rounded Leading Edges (MRLE) at M = 0.40, α = 13°, Re = 3 x 10^6 [[35-17] and Chapter 34].

35.5.3 Effects of Angle of Attack

Experimental pressure distributions for various angles of attack [35-5], see Chapter 19, are shown in Figure 35-25. Up to α = 11.2° only the inner primary vortex exists, and the corresponding suction on the wing surface reaches considerable values near the trailing edge. With increasing angle of attack the outer primary vortex is formed in the rear part of the configuration and its onset point moves upstream with increasing angle of attack. The strength of the inner primary vortex increases up to the region of the onset of the outer primary vortex, but then decreases suddenly downstream towards the trailing edge. This is due to the fact that the vorticity shed from the leading edge is now fed into the outer primary vortex, and this leads to the considerable reduction of the strength of the inner primary vortex. Another effect can also be recognized from Figure 35-25. In that region where an outer primary vortex already exists, the weakened inner primary vortex moves inboard [35-9].

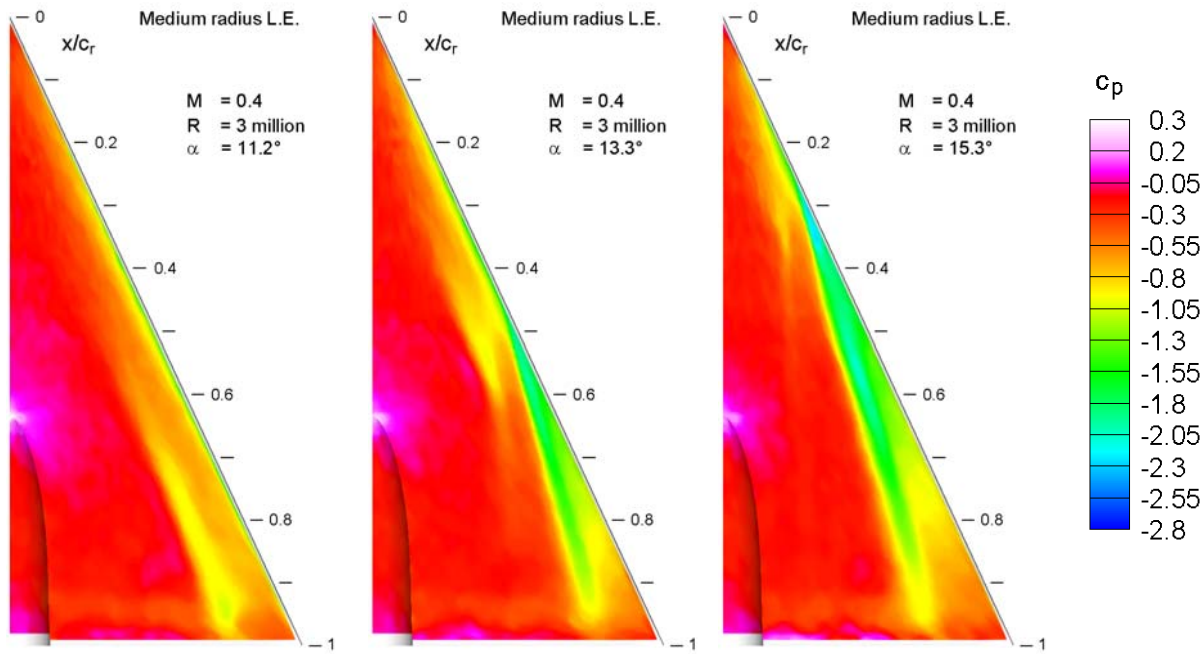

Figure 35-25: Pressure Distributions on the VFE-2 Configuration with Medium Radius Rounded Leading Edges (MRLE) for M = 0.4, R_{mac} = 3 x 10^6 at Various Angles of Attack [[35-5] and Chapter 19].

35.5.4 Effects of Reynolds Number

The vortex formation strongly depends on the Reynolds number [35-5], see Chapter 19. An example is shown in Figure 35-26. With decreasing Reynolds number the onset of the outer primary vortex moves upstream and its strength increases, whereas the inner primary vortex is weakened and its position moves distinctly inboard. Thus, a reduction in Reynolds number has an analogous effect as an increase of the angle of attack according to Figure 35-25, but nevertheless the reasons for this upstream movement of the onset of the outer primary vortex are different for both cases. With increasing angle of attack the adverse pressure gradients on the upper surface of the wing increase as well, and this leads to the upstream movement of the onset of the outer primary vortex. If the angle of attack is unchanged, however, the adverse pressure gradients remain at the same level, but with decreasing Reynolds number the viscous flow is no longer able to stay attached, and this leads again to an upstream movement of the onset of the outer primary vortex [35-9].

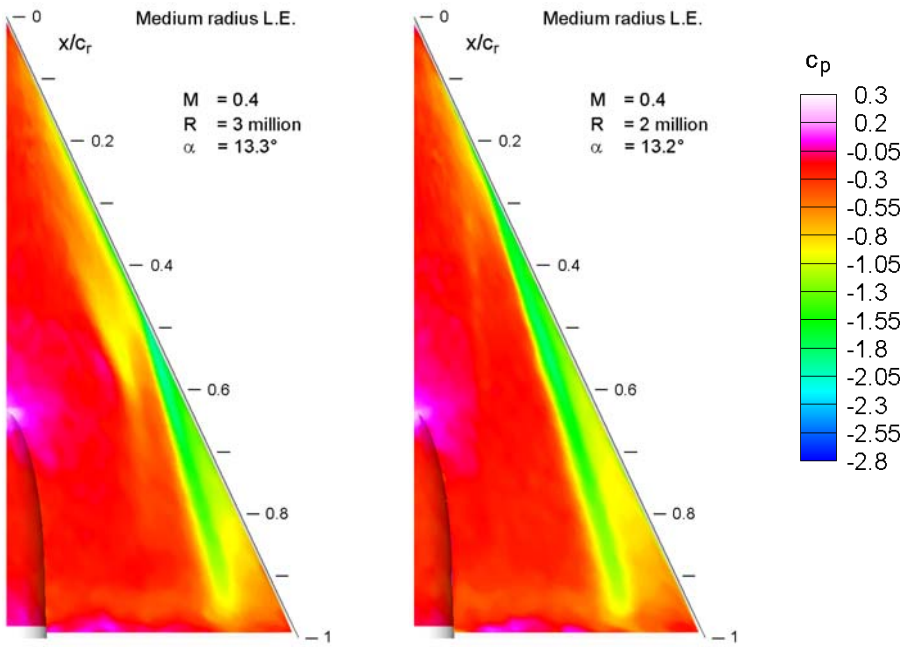

Figure 35-26: Pressure Distributions on the VFE-2 Configuration with Medium Radius Rounded Leading Edges (MRLE) for M = 0.4, α = 13° at Different Reynolds Numbers [[35-5] and Chapter 19].

35.5.5 Effects of Mach Number

In contrasting a subsonic and a transonic Mach number condition, the principal vortex topology remains unchanged, but some compressibility effects can be recognized. In transonic flow the formation of the outer primary vortex starts earlier [35-5], see Chapter 19. Figure 35-27 shows the pressure distributions at α = 13° and $R_{mac} = 2 \times 10^6$ for two different Mach numbers. At the higher Mach number the onset of the outer primary vortex has moved slightly upstream and its axis is distinctly shifted inboard. For M = 0.8 an inner primary vortex has no longer been found. If it exists at all in transonic flow, this vortex must be very weak [35-9].

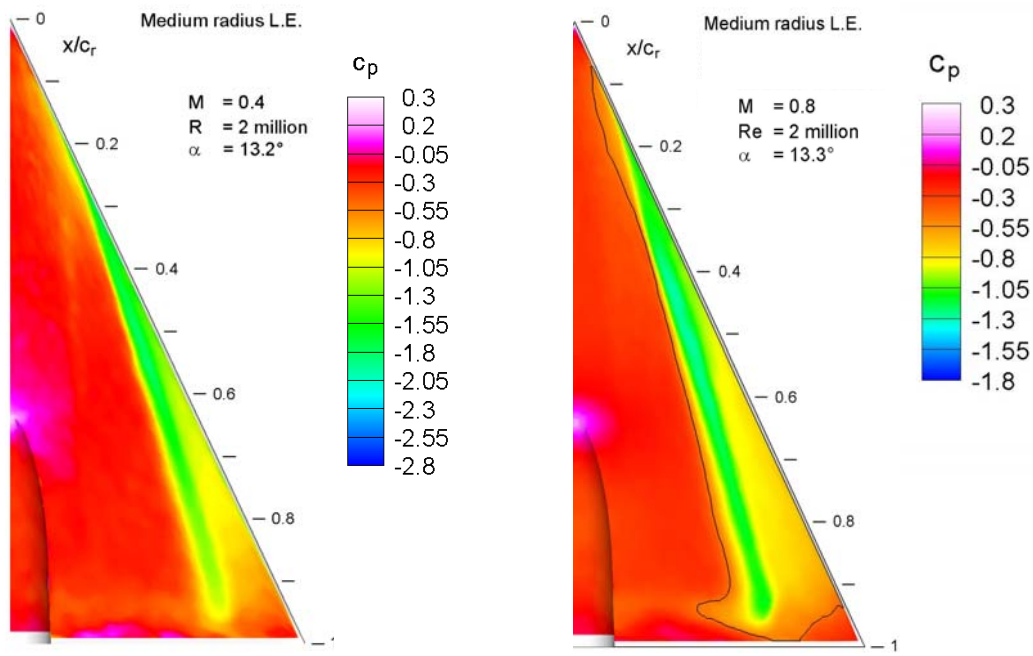

Figure 35-27: Pressure Distributions on the VFE-2 Configuration with Medium Radius Rounded Leading Edges (MRLE) at R_{mac} = 2 x 10^6 and α = 13° for Different Mach Numbers [[35-5] and Chapter 19]. The black line indicates the sonic pressure coefficient.

35.5.6 Understanding of the Flow Physics

Based on the experimental results obtained within the VFE-2 the onset of a vortical flow on the present delta wing with medium radius rounded leading edge can be summarized as follows: at α = 13° the first flow separation takes place in the front part of the wing, where the body is relatively thick. At its very beginning the separated flow region is located close to the body surface, but further downstream a concentrated inner primary vortex is formed quite rapidly. Along the blunt leading edge the curvature radius of the leading edge remains constant, whereas the local half span increases downstream. This means in other words that the leading edge becomes relatively sharper (r_{LE} /b_{loc}) towards the trailing edge of the wing. Correspondingly the suction at the leading edge increases downstream, and finally new flow separations take place in the outer portion of the rear part of the wing, forming an outer primary vortex there. In the region of the onset of this outer primary vortex, strong interference with the already existing inner primary vortex takes place. The dominant part of vorticity, shed from the leading edge, is now fed into the outer primary vortex, whereas the feeding of the inner vortex with vorticity is reduced. Therefore the inner primary vortex decays downstream due to dominating viscous effects.

Unfortunately within VFE-2 not all details of the onset of vortical flow in the front part of the configuration could be investigated experimentally because of geometric constraints of the PIV setup in the wind tunnel, see Chapter 19. However, an important experimental result of the variation of angle of attack, of Reynolds number and of Mach number as described in the previous sections is the fact, that during all movements of the location of the outer primary vortex onset point the two co-rotating vortices were originally connected. The inner primary vortex is present at first, then the outer primary vortex starts, and after its formation the two vortices separate from each other, the outer one increasing in strength and the inner one moving inboard and decaying

downstream through viscous effects. Further experimental investigations of these details may be expected from Glasgow University [35-8], see Chapter 22, where a new wind tunnel model of the VFE-2 configuration came into operation just at the end of the RTO phase of VFE-2.

Due to the encouraging agreement between the experimental and the calculated results related to the two co-rotating primary vortices, see Chapters 25 and 34, further studies of the details of the vortex formation may also be carried out through an analysis of numerical solutions. However, caution is necessary in such an attempt, since the CFD codes themselves are presently not fully validated. Figure 35-28 and Figure 35-29 show latest calculated results on a structured grid by EADS Munich and on an unstructured grid by DLR Braunschweig, and from these numerical results some conclusions may be drawn, which are summarized subsequently and sketched in Figure 35-30.

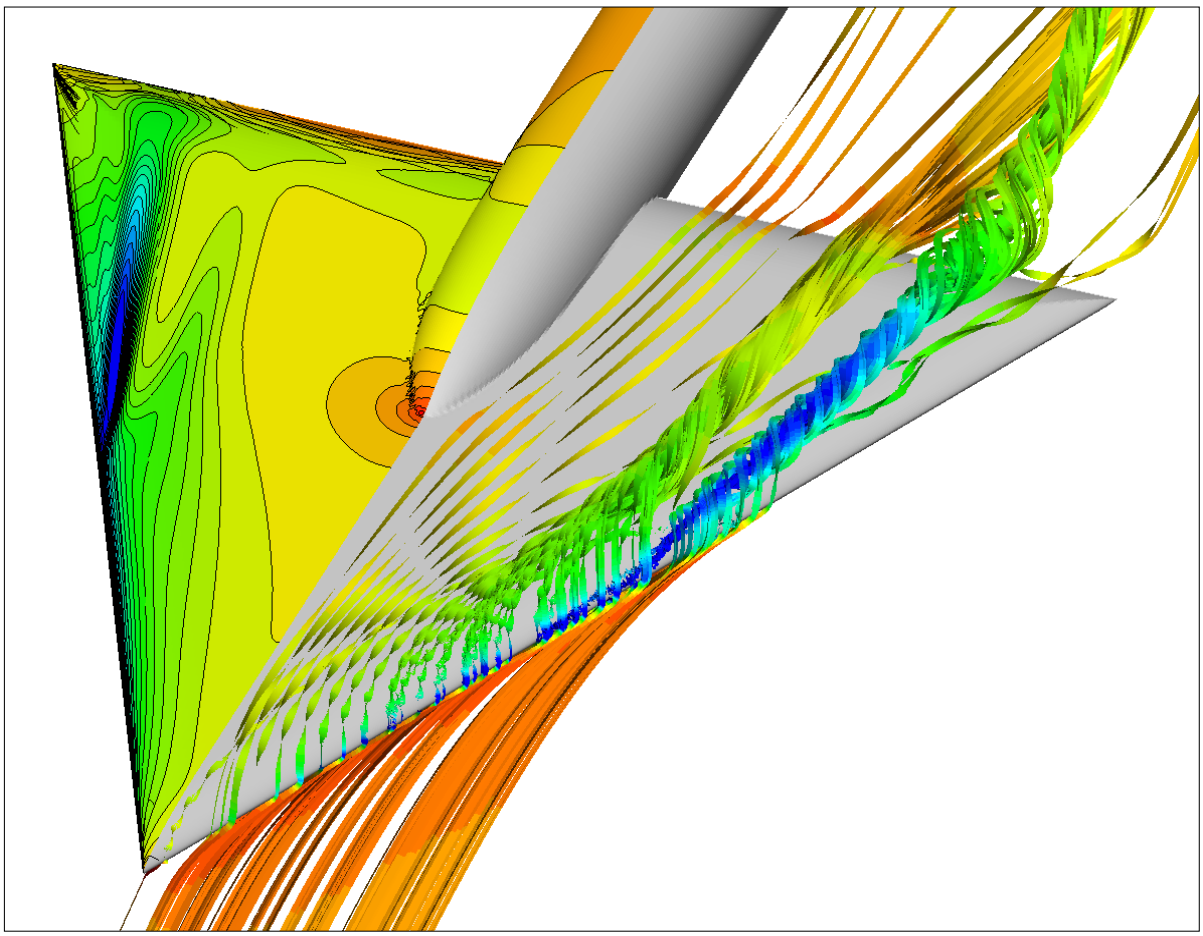

Figure 35-28: Numerical Solution on a Structured Grid for the Flow around the VFE-2 Configuration with Medium Radius Rounded Leading Edges at M = 0.4, R_{mac} = 3 x 10^6, α = 13.3°. Pressure distribution (left) and streamlines in the flow field (right) [[35-11] and Chapter 25].

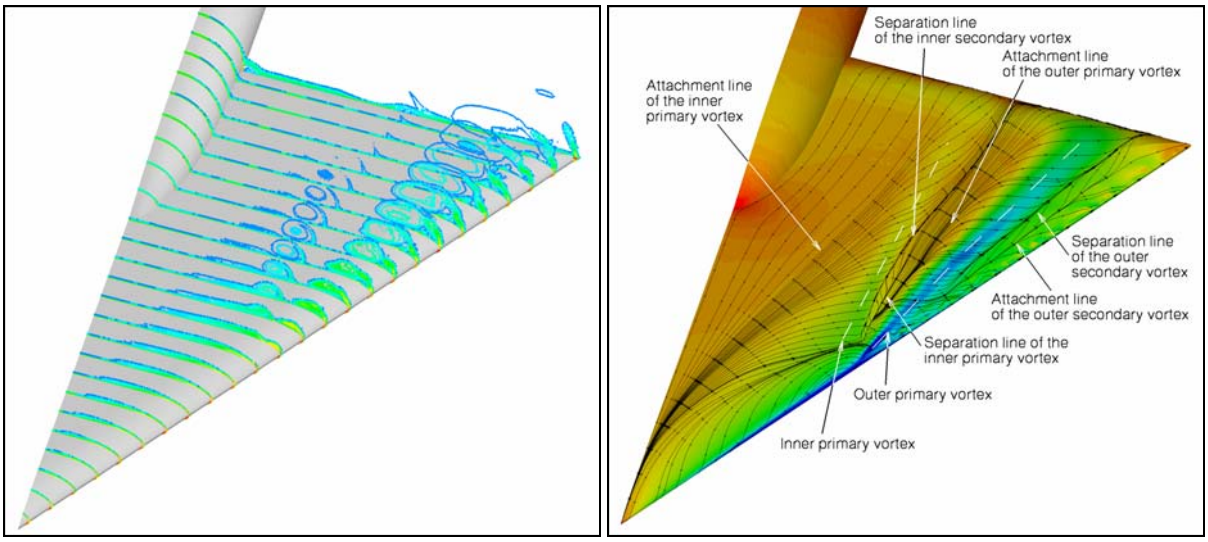

Figure 35-29: Numerical Solution on an Unstructured Grid for the Flow around the VFE-2 Configuration with Medium Radius Rounded Leading Edges at M = 0.4, R_{mac} = 3 x 10^6, α = 13.3°. Distribution of axial vorticity (left) and upper surface friction lines (right) [[35-16] and Chapter 31].

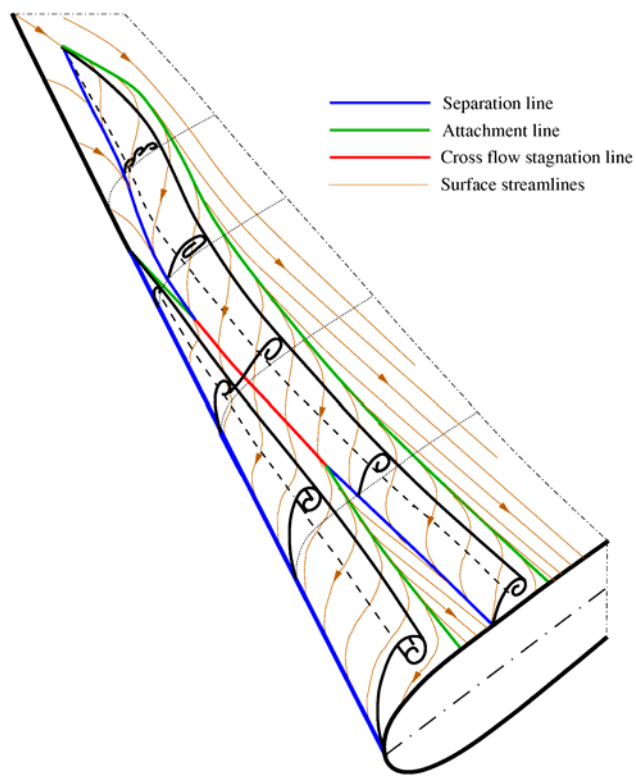

Figure 35-30: Schematic View of the Vortex Formation on the VFE-2 Configuration with Medium Radius Rounded Leading Edge (MRLE) at M = 0.4, R_{mac} = 3 x 10^6, α = 13.3°. According to the Numerical Solutions of EADS [Chapter 25] and DLR [Chapter 31]. (Region between the onset of the outer primary vortex and the separation of the two primary vortices enlarged, secondary vortices omitted).

The first separation due to the thickness distribution of the configuration takes place near the wing apex. The corresponding separation and attachment lines are located far inboard, and according to experimental results [35-5], see Chapter 19, the separated region is thin and broad. According to Figure 35-29 (left) vorticity is distributed over the whole separated region [35-16], see Chapter 31, and a concentrated vortex is not yet present. Underneath the attached flow around the leading edge the primary separation develops and a tiny vortex is formed, marked in both numerical solutions in blue, see Figure 35-28 and Figure 35-29 (right). Due to this small primary vortex the already existing inner flow separation is now set in a new order. The vorticity suddenly concentrates and the inner separation takes the form of an inner primary vortex in the same region where also the outer primary vortex is established. As long as the strength of the outer primary vortex is smaller than that of the inner primary vortex, an attachment line related to the outer vortex and a separation line related to the inner vortex do exist separately. Due to the increasing strength of the outer primary vortex the two lines join and form a cross flow stagnation point, which leaves the wing surface, and correspondingly the outer primary vortex becomes double branched as sketched in Figure 35-30 and the two vortices are connected. More downstream the outer primary vortex becomes dominant. Therefore the free stagnation point in the cross flow between the two vortices approaches the wing again and on the surface it splits up into a separation line corresponding to the inner primary vortex and into an attachment line corresponding to the outer primary vortex. Both vortices are now separated from each other. In this discussion on the conjecturable flow behaviour the secondary vortices related to both primary vortices have not been taken into account, but they could be included into the topology according to Figure 35-30 quite easily.

In future numerical calculations the CFD codes should be validated using the existing experimental data, and if the results are reliable the schematic view of the vortex formation according to Figure 35-30 should be checked, and if necessary corrections should be applied.

35.6 CONCLUSIONS AND OUTLOOK

In the present chapter the results of the Second International Vortex Flow Experiment (VFE-2) have been summarized. The original experimental NASA data base has been considerably enlarged. Significant details of the vortical flow have now been measured. This was accomplished through 15 new wind tunnel experiments coordinated among four countries. A focus was established on two of the leading edges (sharp and medium bluntness) from the NASA experiments, and four new wind tunnel models were fabricated to support the new testing. Surface and off-body measurements, for both steady and fluctuating quantities, have been accumulated using a wide variety of test techniques as well as three-component forces and moments.

The experimental campaigns confirm the multiple-vortex structure of blunt leading edge vortex separation, and considerably more details of this flow are now available through the use of the Pressure Sensitive Paint (PSP) technique. Detailed flow field measurements by Particle Image Velocimetry (PIV) provided new insight into the vortical structure, and surface and off-body fluctuating measurements by Hot-Wire Anemometry (HWA) showed the turbulent structure of these flows.

Within VFE-2 the available CFD codes have been applied to the vortical flow around a relatively simple delta wing configuration with sharp and rounded leading edges. Numerical calculations have been carried out on structured and unstructured grids. The CFD codes have been validated using the experimental data, and the numerical results have been used as guidelines for the set-up of the wind tunnel experiments. Moreover in the final RTO-phase of VFE-2 the numerical results played an important role in the understanding of the flow physics, since the lack of experimental details in some flow regions could be replaced by numerical results. Therefore the present state of knowledge is the outcome of a proper combination of experiments and numerics.

The scientific work of the VFE-2 facet of the RTO AVT-113 Task Group has been carried out from 2003 to 2007 [35-3] as outlined in Chapter 17, and the achieved status of knowledge is described in the present Final Report. As shown in this Chapter 35 many results could be documented, but some problems are still unsolved. Therefore, at the end of the RTO-phase of VFE-2 the scientific program is not terminated. As with VFE-1, the scientific work will continue in the next decade. Many problems have not been solved completely or have even been started, and others have not yet been looked at within the framework of the present Task Group. Therefore new experiments will be carried out worldwide in a new open phase of VFE-2. The configuration under consideration is relatively simple and described analytically, and therefore new wind tunnel models can be built quite easily. Numerical calculations will go on as well, and better results as well as new solutions will be achieved.

The results according to this Final Report will be the starting point for future investigations. In the present resuming Chapter 35 the achievements as well as the unsolved problems have been summarized. On this basis an outlook for the needs of further investigations may be given here.

On the experimental side the needs are:

- Measurements on the boundary layer status laminar/turbulent for the VFE-2 configuration with sharp and rounded leading edges. Fully developed vortical flow without vortex breakdown at $\alpha = 18°$ should be the starting point, and later also partly separated vortical flow at $\alpha = 13°$ could be added. The already existing experimental results will be further evaluated, but there is an urgent need for new measurements.
- Experimental investigations on the shock formation in transonic fully developed vortical flow $\alpha = 23°$ for the VFE-2 configuration with sharp and medium radius rounded leading edges. Subject should be the mutual interference between the terminating and the cross flow shocks on the one hand and vortex breakdown on the other.
- New measurements on the partly separated vortical flow at $\alpha = 13°$. Up to now the structure of the initial flow separation due to the thickness distribution near the apex of the configuration, see Figure 35-30, is unknown. Numerical simulations [35-16] have shown vorticity distributions without a dominating concentrated vortex in this area, see Figure 35-29 and Chapter 31, whereas experiments [35-5] indicate some weak longitudinal vortices in this area, see Figure 35-30 and Chapter 19.

On the numerical side the needs are

- New calculations related to the fully developed vortical flow without vortex breakdown at $\alpha = 18°$ for the VFE-2 configuration with sharp and medium radius rounded leading edges in incompressible flow and at very low Reynolds numbers. Converged solutions should be achieved for various turbulence models, and in comparisons with the available results from Hot-Wire-Anemometry (HWA) [35-7], see Chapter 21, the best suitable turbulence model for calculations of vortical flows should be found.
- Attempts should be made to predict the laminar/turbulent transition in fully developed vortical flows without vortex breakdown at $\alpha = 18°$. Starting point could be the sharp edged VFE-2 configuration. For this purpose two steps would be helpful
    - Calculation of the vortical flow for prescribed laminar and turbulent boundary layer regions on the wing as a guess. A converged solution should be achieved. As input experimental results could be used.
    - Point by point stability analysis of the calculated flow field. Based on the results corresponding modification of the original laminar/turbulent transition guess.

- For partly separated vortical flow at α = 13° the CFD codes should be further validated using the already available or new experimental data. The vortical flow field in the vicinity of the onset point of the outer primary vortex should be analysed in detail in order to check the validity of the schematic view presented in Figure 35-30.

The first RTO-phase of the Second International Vortex Flow Experiment (VFE-2) has been terminated in 2008 by the present Final Report. A second open phase of VFE-2 starts now in 2008. The scientific community is invited to join this project and to start new investigations. Information on the ongoing research may be taken from the new website www.dlr.de/as/vfe-2.

35.7 REFERENCES

[35-1] Chu, J. and Luckring, J.M.: *Experimental Surface Pressure Data Obtained on 65° Delta Wing Across Reynolds Number and Mach Number Ranges*, NASA TM 4645 (1996).

[35-2] Hummel, D. and Redeker, G.: *A New Vortex Flow Experiment for Computer Code Validation*, RTO AVT Symposium "Vortex Flow and High Angle of Attack Aerodynamics", Loen, Norway, 7-11 May 2001, Meeting Proceedings RTO-MP-069 (I), SYA 8-1 to 8-31, 2003.

[35-3] Hummel, D.: *Review of the Second International Vortex Flow Experiment (VFE-2)*, AIAA Paper 2008-0377, 2008.

[35-4] Luckring, J.M.: *Initial Experiments and Analysis of Vortex Flow on Blunt Edged Delta Wings*, AIAA Paper 2008-0378, 2008.

[35-5] Konrath, R., Klein, Ch. and Schröder, A.: *PSP and PIV Investigations on the VFE-2 Configuration in Sub- and Transonic Flow*, AIAA Paper 2008-0379, 2008.

[35-6] Le Roy, J.F., Rodriguez, O. and Kurun, S.: *Experimental and CFD Contribution to Delta Wing Vortical Flow Understanding*, AIAA Paper 2008-0380, 2008.

[35-7] Furman, A. and Breitsamter, Ch.: *Turbulent and Unsteady Flow Characteristics of Delta Wing Vortex Systems*, AIAA Paper 2008-0381, 2008.

[35-8] Coton, F., Mat, S. and Galbraith, R.: *Low Speed Wind Tunnel Characterization of the VFE-2 Wing*, AIAA Paper 2008-0382, 2008.

[35-9] Luckring, J.M. and Hummel, D.: *What was Learned from the New VFE-2 Experiments*, AIAA Paper 2008-0383, 2008.

[35-10] Nangia, R.K.: *Semi-Empirical Prediction of Vortex Onset and Progression on 65° Delta Wings*, RTO-AVT-113, VFE-2 Facet, AIAA Paper 2008-0384, 2008.

[35-11] Fritz, W.: *Numerical Simulation of the Peculiar Subsonic Flow-Field about the VFE-2 Delta Wing with Rounded Leading Edge*, AIAA Paper 2008-0393, 2008.

[35-12] Gürdamar, E., Ortakaya, Y., Kaya, S. and Korkem, B.: *Some Factors Influencing the Vortical Flow Structures on Delta Wings*, AIAA Paper 2008-0394, 2008.

[35-13] Schiavetta, L.A., Boelens, O.J., Crippa, S., Cummings, R.M., Fritz, W. and Badcock, K.J.: *Shock Effects on Delta Wing Vortex Breakdown*, AIAA Paper 2008-0395, 2008.

[35-14] Cummings, R.M. and Schütte, A.: *Detached-Eddy Simulation of the Vortical Flowfield about the VFE-2 Delta Wing*, AIAA Paper 2008-0396, 2008.

[35-15] Crippa, S. and Rizzi, A.: *Steady, Subsonic CFD Analysis of the VFE-2 Configuration and Comparison to Wind Tunnel Data*, AIAA Paper 2008-0397, 2008.

[35-16] Schütte, A. and Lüdeke, H.: *Numerical Investigations on the VFE-2 65-degree Rounded Leading Edge Delta Wing Using the Unstructured DLR-TAU-Code*, AIAA Paper 2008-0398, 2008.

[35-17] Fritz, W. and Cummings, R.M.: *What was Learned from the Numerical Simulations for the VFE-2*, AIAA Paper 2008-0399, 2008.